1. Report No. FHWA/TX-09/0-5261-2	2. Government Accession No.	3. Recipient's Catalog No.
4. Title and Subtitle A METHOD FOR PREDICTING ASPHALT MIXTURE COMPACTABILITY AND ITS INFLUENCE ON MECHANICAL PROPERTIES		5. Report Date December 2008 Published: May 2009
		6. Performing Organization Code
7. Author(s) Eyad Masad, Emad Kassem, Arif Chowdhury, and Zhanping You		8. Performing Organization Report No. Report 0-5261-2
9. Performing Organization Name and Address Texas Transportation Institute The Texas A&M University System College Station, Texas 77843-3135		10. Work Unit No. (TRAIS)
		11. Contract or Grant No. Project 0-5261
12. Sponsoring Agency Name and Address Texas Department of Transportation Research and Technology Implementation Office P. O. Box 5080 Austin, Texas 78763-5080		13. Type of Report and Period Covered Technical Report: January 2008-August 2008
		14. Sponsoring Agency Code

16. Abstract

This project aimed at providing better understanding of the factors affecting the uniformity and level of compaction; and the performance of asphalt pavements. TxDOT research report 0-5261-1 documented some of the findings of this research project. This research report documents the efforts and findings of experiments conducted with more test sections. In the first phase of this report, a number of field test sections were compacted, and field cores were extracted. These cores were scanned using X-ray Computed Tomography (X-ray CT) to capture the air void distributions in these cores. The air void distribution correlated well with the compaction effort across the mat. The compaction effort was found to be a function of the number of roller passes and the relative location of each pass across the mat. The Compaction Index (CI) developed in the TxDOT research report 0-5261-1 was used to quantify the compaction effort at any point in the pavement. This index combines the number of roller passes along with the effectiveness of each pass on the mat. The compactability of asphalt mixtures in the field correlated well with compactability of asphalt mixtures in the laboratory. The CI was used to quantify the compactability of asphalt mixtures in the field while the slope of the compaction curves obtained from Superpave Gyratory Compactor was used to quantify the compactability of asphalt mixtures in the laboratory.

In the second phase of this report, the effect of different levels of compaction on the performance of asphalt mixtures was studied using a fracture mechanics approach and DEM models. The results showed that test specimens with less percent air voids performed better than the ones with higher percent air voids. In addition moisture-conditioned specimens performed worse than the dry ones at the same compaction levels. Furthermore, guidelines were developed to assist in predicting the compactability in the field based on laboratory measurements during the mixture design stage; and to improve the field compaction.

17. Key Words Hot-Mix Asphalt, Compaction, Effectiveness Factor, Uniformity, X-ray CT, HMA Moisture Susceptibility, DEM	18. Distribution Statement No restrictions. This document is available to the public through NTIS: National Technical Information Service Springfield, Virginia 22161 http://www.ntis.gov	
19. Security Classif. (of this report) Unclassified	20. Security Classif. (of this page) Unclassified	21. No. of Pages 98	22. Price

A METHOD FOR PREDICTING ASPHALT MIXTURE COMPACTABILITY AND ITS INFLUENCE ON MECHANICAL PROPERTIES

by

Eyad Masad
Associate Research Scientist
Texas Transportation Institute

Emad Kassem
Assistant Research Scientist
Texas Transportation Institute

Arif Chowdhury
Assistant Research Engineer
Texas Transportation Institute

and

Zhanping You
Associate Professor
Michigan Technological University

DISCLAIMER

The contents of this report reflect the views of the authors, who are responsible for the facts and the accuracy of the data presented herein. The contents do not necessarily reflect the official view or policies of the Texas Department of Transportation (TxDOT) or the Federal Highway Administration (FHWA). This report does not constitute a standard, specification, or regulation. The engineer in charge of the project was Eyad A. Masad, Texas #96368.

ACKNOWLEDGMENTS

TABLE OF CONTENTS

LIST OF FIGURES

LIST OF TABLES

CHAPTER 1
INTRODUCTION AND BACKGROUND

OVERVIEW

Compaction is the process by which the volume of an asphalt mixture is reduced, leading to an increase in unit weight of the mixture and interlock among aggregate particles (Corps of Engineers 2000; Roberts et al. 1996). The performance of asphalt mixtures is significantly influenced by the degree of compaction. Insufficient compaction leads to poor asphalt pavement performance even if all desirable mixture design characteristics are met. Poor compaction can result in premature permanent deformation or rutting, excessive aging, and moisture damage.

There are many factors that affect the compaction process; these factors include the properties of the materials in the mixture, environmental variables, conditions at the lay down site, and the method of compaction. A number of studies were carried out in order to evaluate the relationship between laboratory and field compaction methods and mechanical properties of asphalt mixtures (Consuegra et al. 1989; Harvey and Monismith 1993; Peterson et al. 2004; Tashman et al. 2001). Based on the published literature, it can be seen that very little effort has been devoted in the past to evaluate the effect of changes in field compaction patterns on degree of compaction and uniformity of air void distribution in asphalt pavements. This uniformity leads to asphalt pavements with more uniform properties and improved performance. Additionally, there is a need to develop a method to relate field compaction to laboratory compaction in order to predict asphalt mixture compactability based on laboratory measurements.

The effect of the air void distribution on moisture diffusion, as an important cause of moisture damage in asphalt pavements, also needs to be investigated. Most studies have focused on permeability as a measure of the infiltration of water in the mixture (Masad et al. 2006a). However, evidence of severe moisture damage in pavements in areas with low levels of annual rainfall, such as Arizona and New Mexico (Caro et al. 2007), implies that the diffusion of water vapor could be an important source of moisture damage in pavements. The diffusion coefficient is an important input for modeling moisture transport and predicting moisture damage in asphalt mixtures. Developing an

1

experimental procedure for measuring the diffusion coefficient of asphalt mixtures and evaluating the effect of the air void distribution on the moisture diffusion is one of the objectives of this study.

Percent and size of air voids are important factors that influence asphalt mixture mechanical properties. However, experimental and modeling techniques are needed to quantify the relationship between air void distribution and mechanical properties. These techniques can then be used to design mixtures with desirable mechanical properties.

PROBLEM STATEMENT AND OBJECTIVES

The degree of compaction has a significant influence on asphalt mixture performance in the field. Providing all desirable mixture design characteristics without adequate compaction will lead to poor asphalt pavement performance. Poor compaction has been associated with premature permanent deformation or rutting, excessive aging, and moisture damage. There is no method currently available to assess the compactability of asphalt mixtures in the field based on laboratory measurements. A few studies were carried out in the past to study the effect of changes in field compaction patterns on mechanical properties and degree of compaction and air void distribution in asphalt pavements. This study aimed at providing better understanding of the compaction factors that influence uniformity and degree of compaction and resulting mechanical properties of asphalt mixtures. This understanding is necessary in order to compact more uniform asphalt pavements with improved performance. In addition, this study investigated the effect of air void distribution on moisture diffusion. Moisture diffusion is one of the important modes of moisture damage that might occur as a result of poor compaction. The effect of air void on the performance of asphalt mixtures was investigated using a fracture mechanics approach and Discrete Element Models (DEM).

Two research reports documents the efforts and findings of TxDOT Research Project 0-5261. The first report (0-5261-1, Masad et al. 2008) covered the following topics:

1) Develop a method to quantify the level of pavement compaction and its uniformity,

2) Predict degree of compaction in the field based on laboratory measurements,

3) Determine the influence of different compaction patterns on asphalt pavement uniformity,

4) Determine the influence of air void distribution on the response of asphalt mixtures using the overlay tester and Hamburg device,

5) Develop a test procedure for measuring moisture diffusion in asphalt mixtures.

This second report (0-5261-2) complements the first report by covering the following topics:

1) Validate the findings from Report 0-5261-1 (Masad et al. 2008) in regard to the development of a method "Compaction Index (CI)" to assess field compactability of asphalt mixtures using further field and laboratory experiments,

2) Validate the findings from Report 0-5261-1 in regard to the development of a method to predict field compactability using laboratory measurements,

3) Develop a fracture mechanics approach to assess moisture damage in asphalt mixtures and its relationship to air void distribution,

4) Employ the DEM to study the effect of the air void on some mechanical properties of asphalt mixtures,

5) Develop a guideline for improving the field Hot Mix Asphalt (HMA) compaction.

STUDY PLAN

The objectives of this research project were achieved by executing the tasks described in the following sections.

Task 1: Conduct Field Compaction

Roadway projects with different types of mixtures were identified. Field cores were extracted from the test sections. Number of passes and the position of each compactor's pass were

3

recorded across the mat, and their influence on measured percent air voids in the recovered field cores was studied. The data and samples collected during the field projects include:

- ambient, surface, and mixture temperature;
- density data measured using nuclear and non-nuclear density gauges;
- equipment used in the project, (screed, dump truck, or materials transfer device, roller): size, weight, pattern, sequence, number of passes, etc.;
- cores for Saturated Surface Dry (SSD) density, vacuum sealed density, X-ray CT, and performance testing; and
- plant mixture and virgin aggregate and binder for further testing.

Task 2: Analyze Air Void Distribution

X-ray Computed Tomography (CT) was used to capture the internal structure of asphalt mixtures. The CT images were analyzed using image analysis techniques (Image-Pro® Plus software 1999). Three-dimensional maps of air void distribution in pavement sections were generated by inputting percent air voids as a function of depth (from X-ray CT images) and the location of cores in the pavement to the Matlab 7.1 software (2004). This application is considered valuable because it provides an estimate of percent air voids at any point in the pavement section every 1 mm of depth. As such, one can determine the detailed three-dimensional distribution of air voids. The uniformity of air void distribution was quantified using mathematical indices.

Task 3: Evaluate Field Compactability and Laboratory Compactability

In the field, the location of the compactors across the mat during the compaction process was recorded for each pass by measuring the distance from the edge of the compactor with respect to the longitudinal joint of the mat. The compactability of asphalt mixtures in the field was evaluated by considering the number of passes of the rollers and the relative location of each pass. In the laboratory, a number of laboratory Superpave Gyratory Compactor (SGC) specimens were compacted for the same asphalt mixtures studied in the field. The compactability of the laboratory mixtures was quantified by determining the slope of the percent air voids to number of gyrations on a logarithmic scale for each sample at a certain percent air voids. The compactability of asphalt

mixtures in the laboratory was compared to the compaction index (CI) which quantifies the compactability of the same mixtures in the field.

Task 4: Use Fracture Mechanics Approach to Assess Moisture Damage

The effect of air voids in asphalt mixtures on moisture susceptibility was evaluated using a fracture mechanics approach that accounts for fundamental material properties. Asphalt mixture samples with different percent air voids were prepared. Test samples were subjected to dynamic loading under two different conditions: dry (unconditioned) and wet (moisture-conditioned). The crack growth index developed by Lytton et al. (1993) and later modified by Masad et al. (2006b) and Arambula (2007) was employed in order to assess moisture susceptibility of asphalt mixtures. The parameters required for the crack growth index were obtained through a relaxation modulus test, a tensile test, a dynamic tensile test, and surface energy tests.

Task 5: Use DEM to Study Effect of Air Void on Mechanical Properties of Asphalt Mixtures

This task focused on studying the air void effect on the Young's modulus of asphalt mixtures using Discrete Element Models (DEM). In this task, laboratory specimens and field cores were scanned using X-ray CT to obtain the microstructure of the air void levels. Two-dimensional and three-dimensional DEM models were developed to evaluate the performance of the mixtures.

Task 6: Develop Guideline for Improving Field Compaction

Researchers submitted recommendations based on the findings of this study in order to compact more uniform asphalt mixtures in the field and to assess the compactability of asphalt mixtures in the field based on laboratory measurements. The findings of the compactability of asphalt mixtures would be useful in achieving the desired compaction levels in the field.

ORGANIZATION OF REPORT

This report documents the research efforts outlined in Tasks 1 through 6. Chapter 1 presents the overview, problem statement, objectives, and the list of tasks conducted

under this research project. Chapter 2 provides a brief description of the field projects, field testing conducted in later part of the research project, and analyses of the uniformity of air void distribution and the compactability of asphalt mixtures. Chapter 3 discusses the fracture mechanics approach and the experimental tests used to assess the moisture damage of asphalt mixtures with different percent of air voids. Chapter 4 reports the efforts for studying the air void effect on the behavior of asphalt mixtures using DEM. Chapter 5 introduces a brief guideline for improving the compaction of HMA mixture in the field and decreasing the effort required to achieve desired field compaction. Finally, Chapter 6 presents the overall conclusions and recommendations.

CHAPTER 2
EVALUATION OF FIELD COMPACTION

INTRODUCTION

As part of Task 2 and 3 outlined in Chapter 1, the research team identified and conducted testing as part of 14 field HMA compaction projects in Texas. The first report published from this project documented the research efforts and their findings from the first 11 projects. This chapter documents the findings from the last three field projects that were conducted in 2008.

DESCRIPTION OF TEST SECTIONS

Test sections from three field projects were evaluated with the help of the TxDOT. These test sections were part of SH 44 in the Laredo District, SH 6 in the Bryan District, and SL 1 (Mopac Highway) in the Austin District. The compaction pattern was not modified from the one established by the contactor in these construction projects. The researchers recorded field compaction effort; conducted tests in the field; obtained field cores, plant mix, and virgin materials; and conducted laboratory tests on laboratory compacted specimens and field cores. These test sections were studied to evaluate the findings reported in Report 0-5261-1 (Masad et al. 2008). Table 2-1 provides a brief description of mixtures used in these field projects; Table 2-2 summarizes the compaction patterns. The following paragraphs briefly describe the research efforts and construction projects included in this report.

SH 6 in Bryan District

This construction site was located south of Hearne in Robertson County in the Bryan District. The test was conducted on the southbound outside lane in June 2008. Both sides of the HMA mat were restrained. The contractor, Knife River Corporation, placed 2-inch thick Stone Matrix Asphalt (SMA) after milling off the existing layer. Before placement of SMA they applied tack coat. This SMA mixture was designed using sandstone, limestone, and mineral filler with 6.4 percent PG 76-22 binder. This SMA layer was again covered with one layer of seal coat and PFC. The research team

7

concentrated only on the compaction of SMA layer. Figure 2-1 shows the coring layout on SH 6.

Table 2-1. Summary of Mixture Designs.

Highway ID	Mixture Type	Date of Field Testing	Aggregate (Major)	Binder	Optimum AC %	Max Rice Sp Gr.	VMA at Op. AC.	Design Air Void, %
SH 44 LRD	Type B	Jan 2008	Siliceous River Gravel	PG 76-22	4.2	2.443	13.5	4
SH 6 BRY	SMA	June 2008	Sandstone & Limestone	PG 76-22	6.4	2.419	17.5	3
SL 1 AUS	SMA	June 2008	Sandstone & Limestone	PG 76-22	6.2	2.352	17.5	4

Table 2-2. Description of Compaction Patterns.

Highway ID	Compaction Pattern		
	BD	IM	FS
SH 44 LRD	Steel Wheel Vibratory	Steel Wheel Static	Pneumatic Wheel
SH 6 BRY	Steel Wheel Vibratory	N/A	Steel Wheel Static
SL 1 AUS	Steel Wheel Vibratory	N/A	Steel Wheel Static

BD: Breakdown, IM: Intermediate, FS: Finish

SH 44 in Laredo District

This construction site was located about 1 mile east of Freer in Duvall County of the Laredo District. The test was conducted on the eastbound outside lane and shoulder in January 2008. The inside edge of the HMA mat was restrained while the outside edge was unrestrained. Hass Anderson, the contractor of this project, placed a 2-inch thick Type B mixture on a recently constructed flexible base. The contractor also applied a prime coat on the flexible base right before the placement of a Type B mixture as shown

8

in Figure 2-2. Finally one course seal coat layer was placed on the HMA surface as a final surface. The research team was focused only on the compaction of the HMA layer. This Type B mixture included primarily crushed river gravel with a 4.2 percent PG 76-22 binder.

Figure 2-1. Coring Layout on SH 6.

SL 1 in Austin District

This construction site was located in the City of Austin in the Austin District. It was an SMA overlay project. The test was conducted on the southbound outside lane in June 2008. Both sides of the HMA mat were restrained. Earlier the existing surface layer was milled off, followed by placement of a one-layer seal coat. Due to high traffic volume, the entire paving of this project was completed at night. This SMA mixture was designed using sandstone, limestone, fly ash, and limestone screening with 6.2 percent PG 76-22 binder.

Figure 2-2. Application of Prime Coat on Flexible Base.

RELATIONSHIP BETWEEN COMPACTION EFFORT AND PERCENT AIR VOIDS

In each of the field projects, the research team recorded the number of roller passes and their relative locations during each pass. Field cores were obtained from different locations of the paving mat (white circles in Figure 2-1). The percent air voids of the extracted field cores were measured using the Saturated Surface Dry (SSD) Procedure (AASHTO 2002a). The number of passes of each compaction roller was plotted along with the percent air voids across the test section. The percent air voids represents the average percent of air voids of at least two cores taken longitudinally at a given distance from the pavement section edge. Figures 2-3 through 2-5 show the results of the test sections.
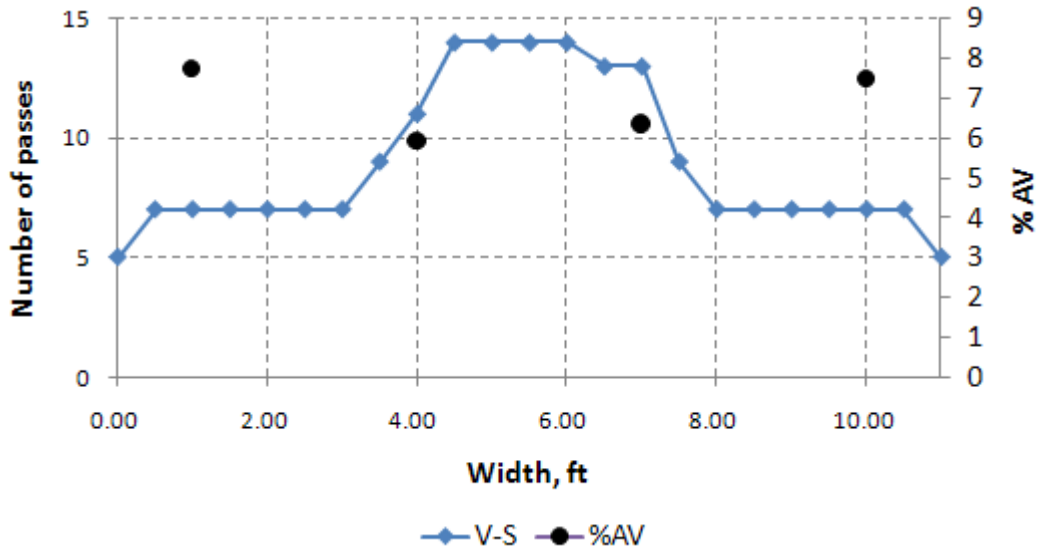
Note: Breakdown roller: vibratory and static (V-S), finish roller: static (S). The static roller was applied after the mat cooled down and not included herein.

Figure 2-3. Number of Passes and the Percent of Air Voids across the Mat in SH 6 Test Section.
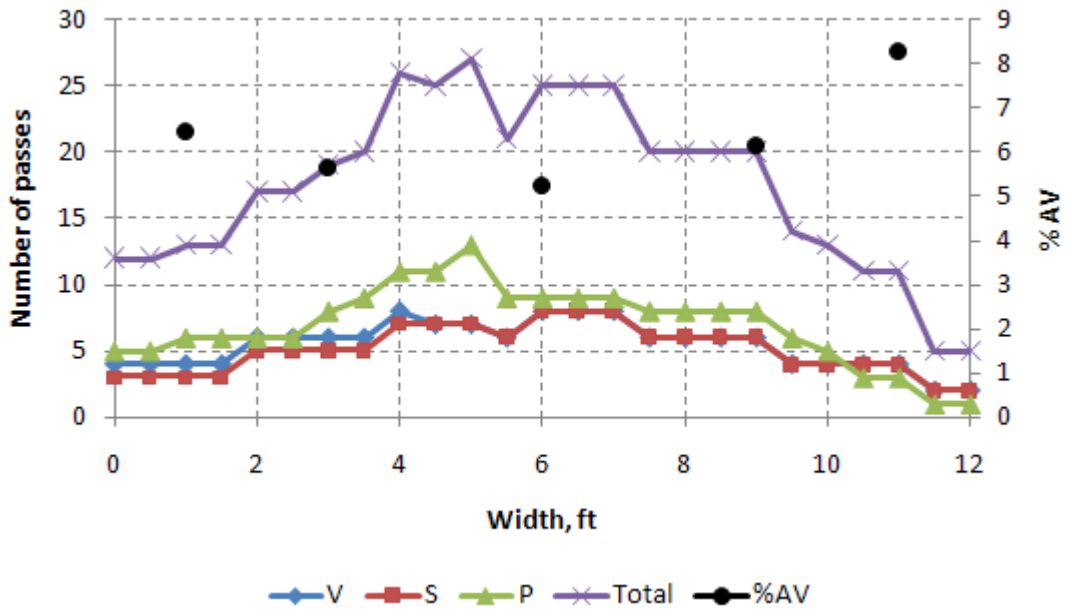
Note: Breakdown roller: vibratory (V), intermediate roller: static (S), finish roller: pneumatic (P).

Figure 2-4. Number of Passes and the Percent of Air Voids across the Mat in SH 44 Test Section.
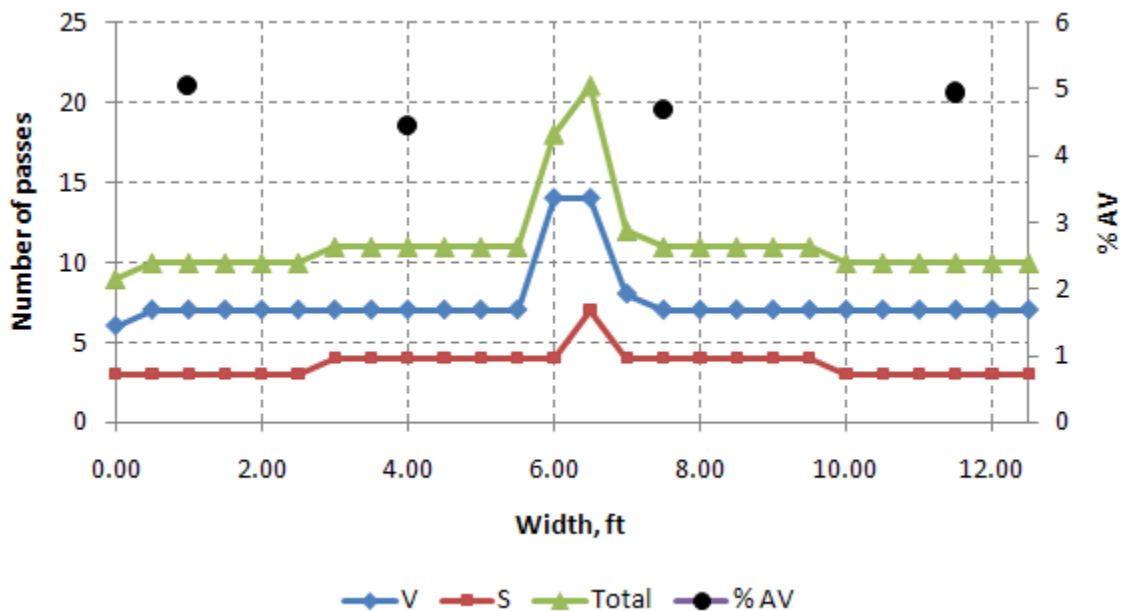
Note: Breakdown roller: vibratory (V), finish roller: static (S).

Figure 2-5. Number of Passes and the Percent of Air Voids across the Mat in SL 1 Test Section.

In Report 0-5261-1 (Masad et al. 2008), an index termed Compaction Index (CI) was developed. The CI is a function of number of passes at a point and the position of the point with respect to the compaction roller width. The efficiency of compaction (reducing air voids) at a given point on a paving mat was found to be a function of the location of this point with respect to the roller compactor width. The effectiveness of one pass across the roller width is shown in Figure 2-6. A point on the mat closer to the center of the roller is subjected to more effective compaction than a point closer to the edge of the roller. The percent air voids was plotted against the summation of number of passes multiplied by the effectiveness factor corresponding to each pass. This summation is termed CI. The CI correlated very well with the percent air voids for the test sections evaluated in Report 0-5261-1. The air voids of a point on the mat are plotted against the number of roller passes and against CI calculated for that particular point. These plots are shown in Figures 2-7 through 2-9 for SH 5, SH 44, and SL 1, respectively.

Figure 2-6 Effectiveness Distribution across Roller Width.
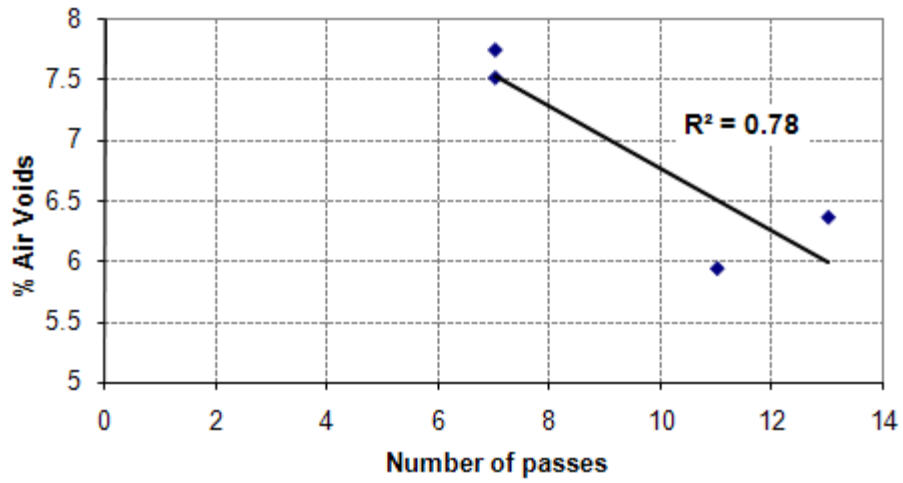
(a)
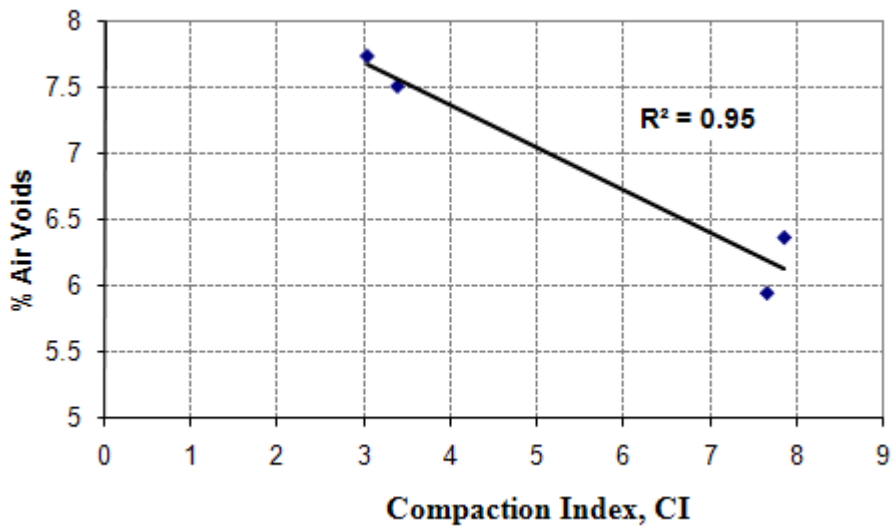
(b)

Figure 2-7. (a) Number of Passes versus the Percent of Air Voids in SH 6 Test Section, (b) Compaction Index versus the Percent of Air Voids in SH 6 Test Section.
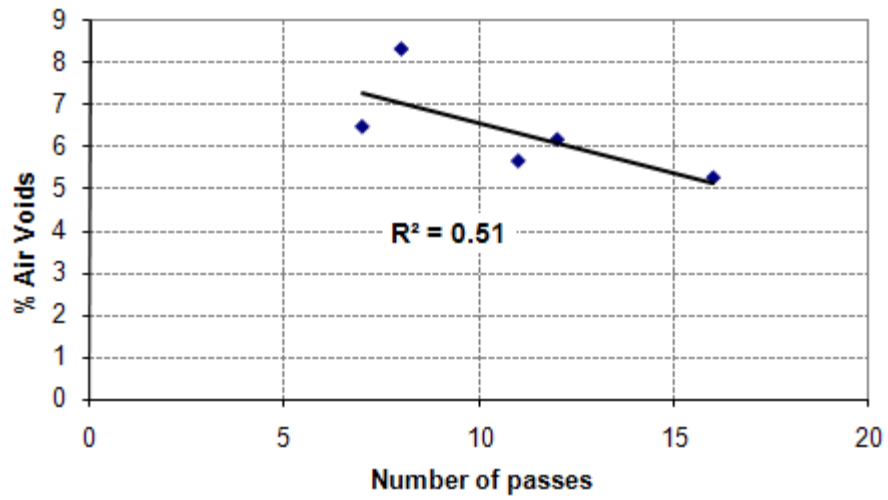
(a)
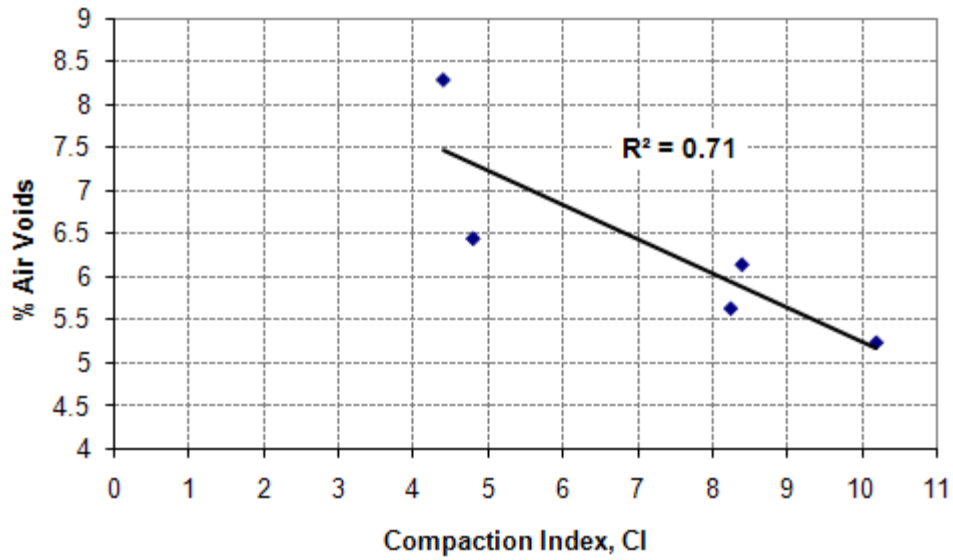
(b)

Figure 2-8. (a) Number of Passes versus the Percent of Air Voids in SH 44 Test Section, (b) Compaction Index versus the Percent of Air Voids in SH 44 Test Section.
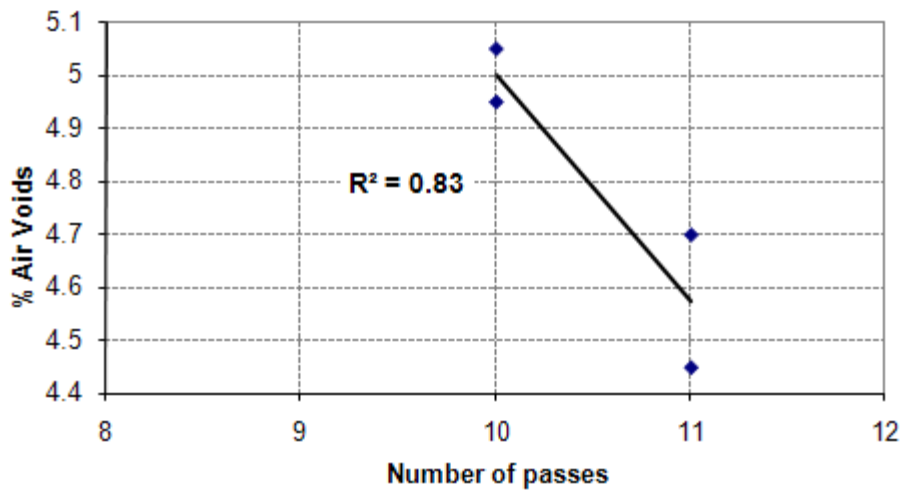
(a)
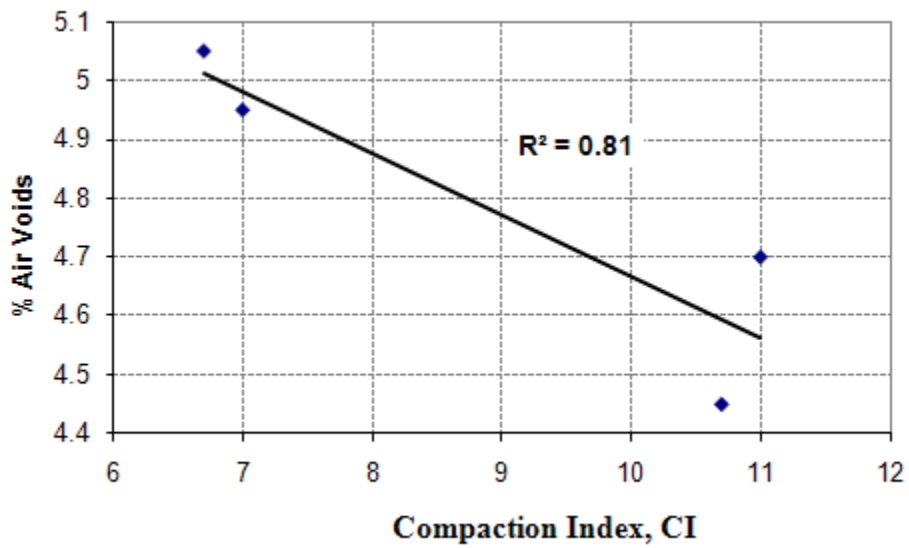
(b)

Figure 2-9. (a) Number of Passes versus the Percent of Air Voids in SL 1 Test Section, (b) Compaction Index versus the Percent of Air Voids in SL 1 Test Section.

APPLICATIONS OF THE COMPACTION INDEX

In Report 0-5261-1, it has been found that uniform percent air voids across the mat corresponded to uniform CI. This point is illustrated herein in Figures 2-10 through 2-12. These figures (upper part) were generated by inputting the location of each core and its percent air voids to the Matlab 7.1 software (2004). Then an interpolation algorithm in Matlab was employed to predict percent air voids in the whole test section. The bottom part of each graph indicates the potential of acquiring uniform air void distribution by achieving uniform CI across the mat.

The compactability of given asphalt mixtures in the field can be predicted based on laboratory measurements. The CI, calculated based on field compaction data, was plotted against corresponding percent air voids for different asphalt mixtures. Figure 2-13 shows such a relationship including the field projects in this report and those evaluated in Report 0-5261-1 (Masad et al. 2008). In the laboratory, four SGC specimens (150 mm diameter and approximately 63.5 mm in height) were fabricated at a 1.25° gyration angle, and two specimens were compacted at a 2.0° gyration angle from different asphalt mixtures. The slope of percent air voids to number of gyrations in logarithmic scale was calculated. Figure 2-14 shows the relationship between the average slope calculated from the initial compaction point to the point of 8 percent air voids in the laboratory versus the CI at this percent air voids for all asphalt mixtures included in this project. Mixtures with higher slope in the laboratory needed less CI in the field (less compaction effort). This relationship offers the potential to estimate the required compaction effort in the field (i.e., CI) based on the slope of number of gyrations and percent air voids in the laboratory. It should be pointed out that the compactability of SH 44 at 8 percent air voids could not be assessed in the field since the extracted cores have relatively low percent air voids.

17

(a)

(b)
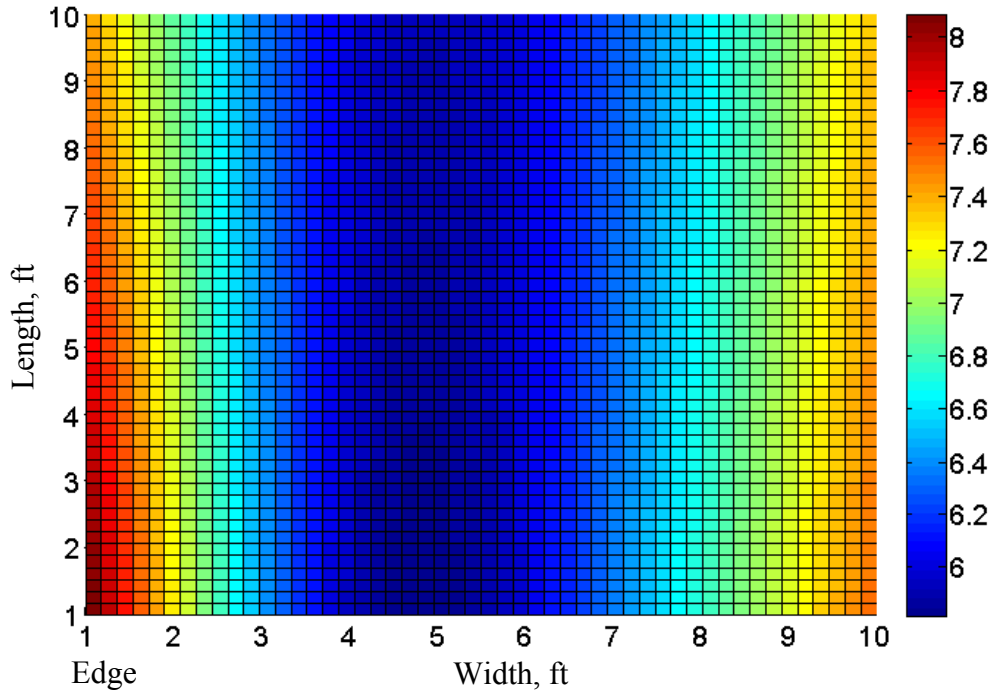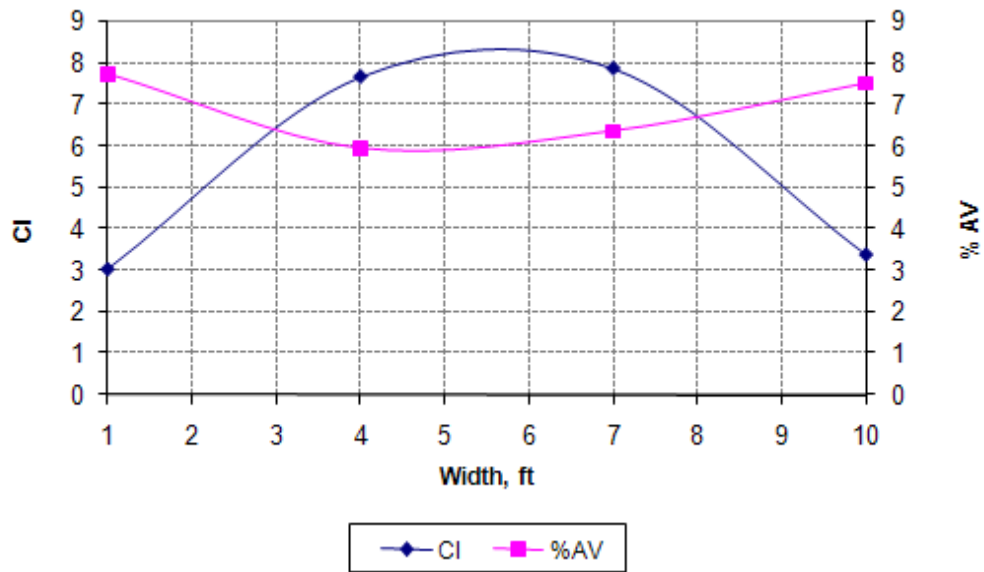
Note: The total width of the mat is 11 ft.

Figure 2-10. (a) Air Void Distribution (%) across the Mat for SH 6 Test Section, (b) the CI and Average Percent of Air Voids across the Mat for SH 6 Test Section.

18

(a)

(b)
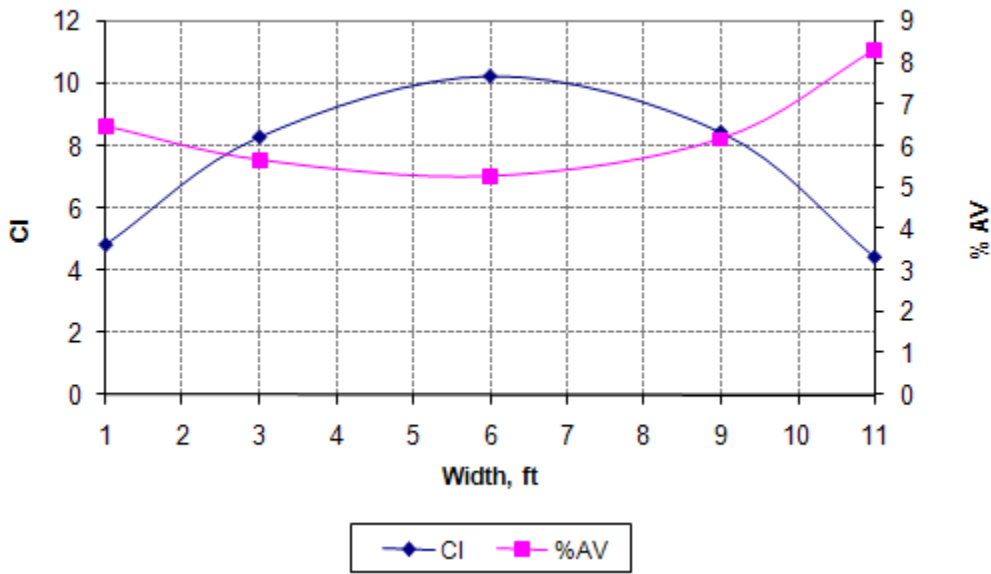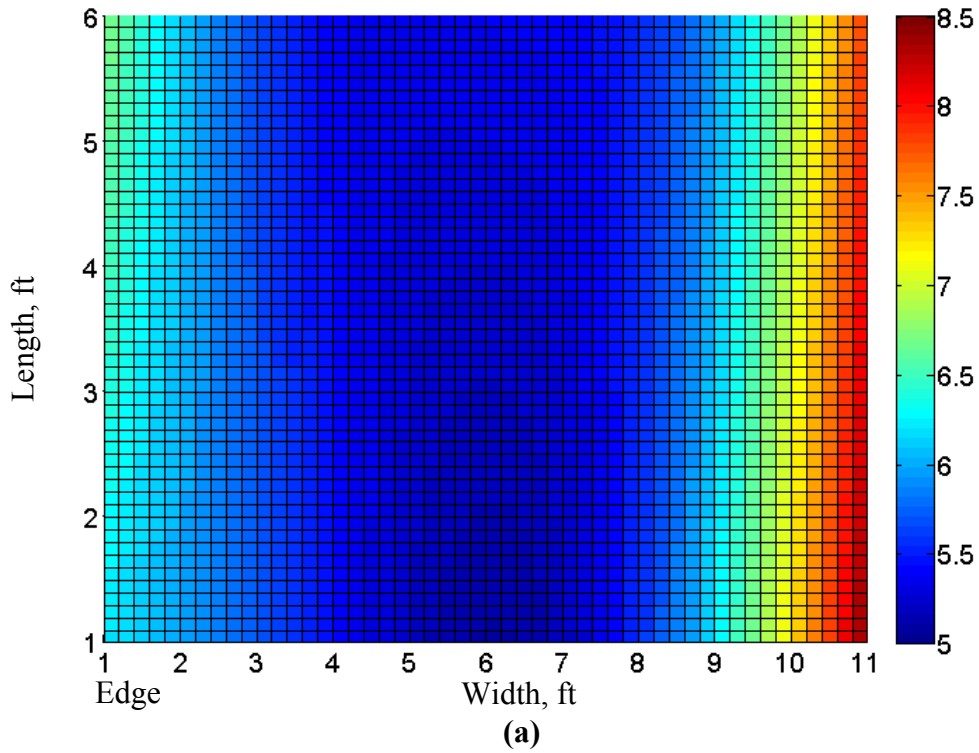
Note: The total width of the mat is 12.0 ft.

Figure 2-11. (a) Air Void Distribution (%) across the Mat for SH 44 Test Section, (b) the CI and Average Percent of Air Voids across the Mat for SH 44 Test Section.

(a)

(b)
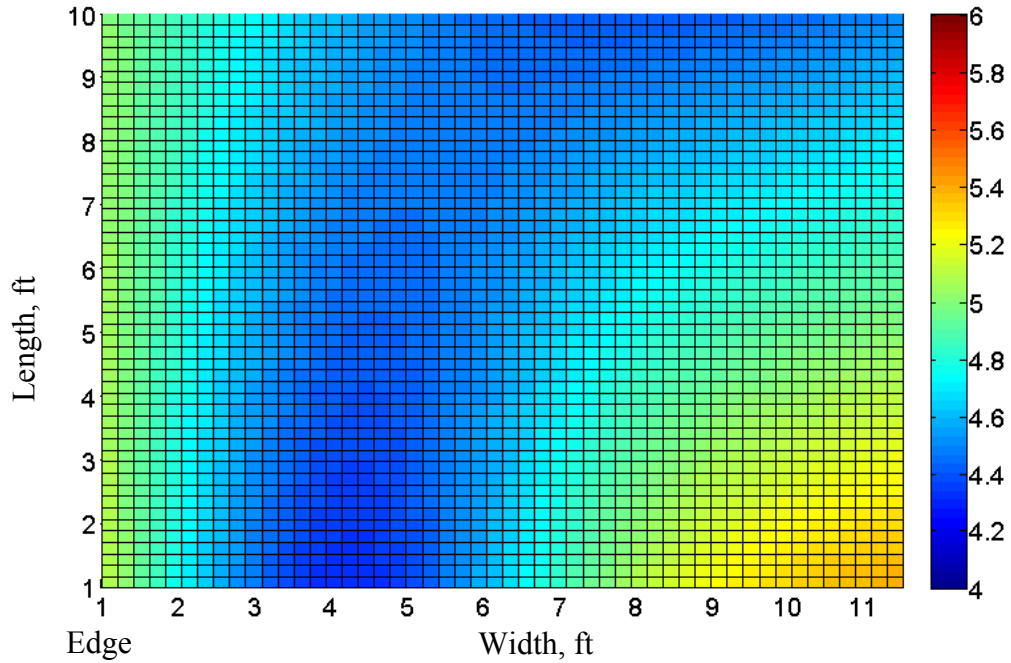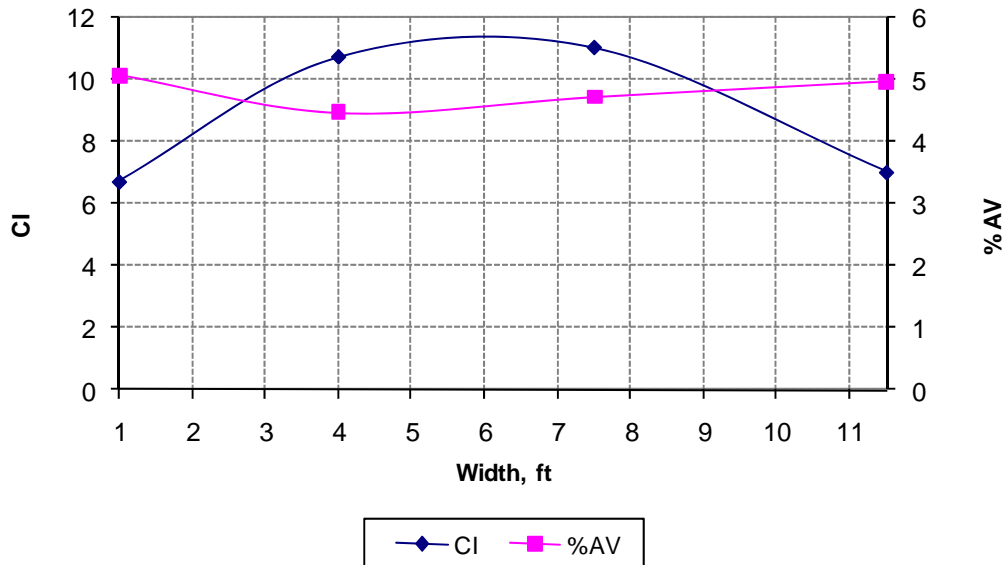
Note: The total width of the mat is 12.5 ft.

Figure 2-12. (a) Air Void Distribution (%) across the Mat for SL 1 Test Section, (b) the CI and Average Percent of Air Voids across the Mat for SL 1 Test Section.
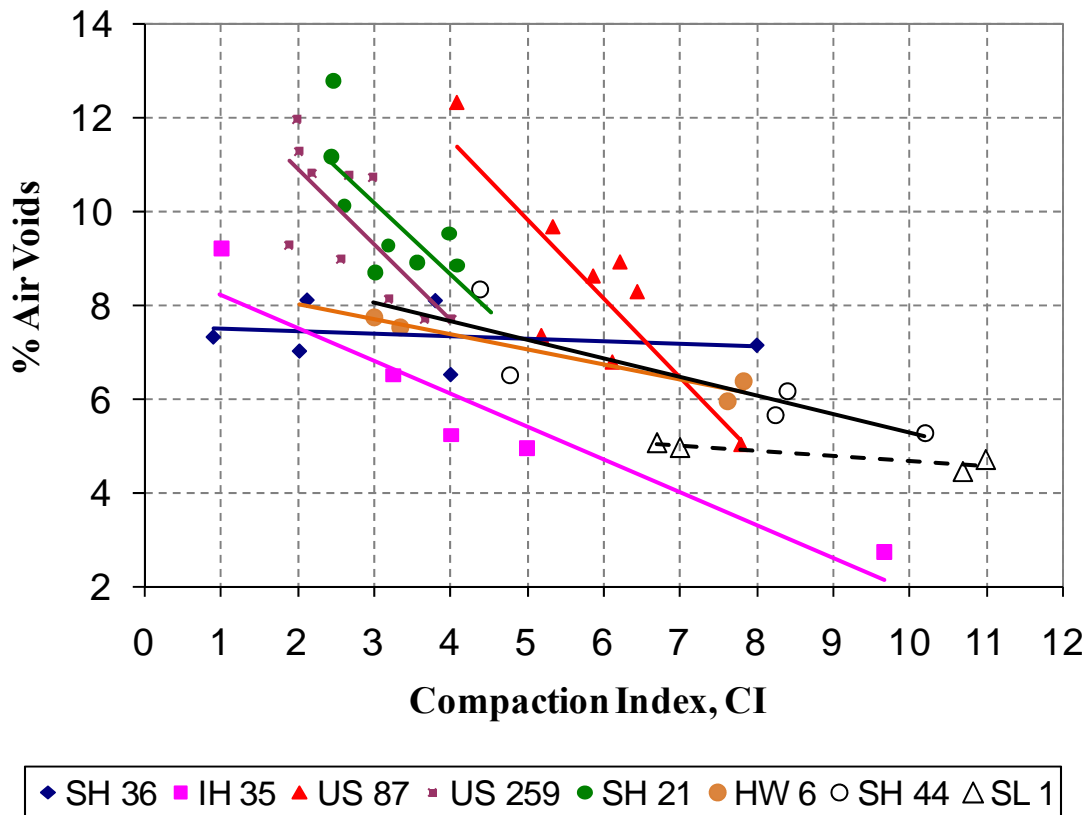
Figure 2-13. The CI versus the Percent of Air Voids.

In Report 0-5261-1, three-dimensional maps of air void distribution in pavement sections were generated by inputting percent air voids as a function of depth (from X-ray CT images) and the location of cores in the pavement to the Matlab 7.1 software. This application were found to be useful as it provides an estimate of percent air voids at any point in the pavement section, every 1 mm of depth. As such, one can determine the detailed three-dimensional distribution of air voids.

Figures 2-15 through 2-17 show examples of the vertical distribution of air voids in pavement sections. The results of these test sections confirmed the findings of Report 0-5261-1 where the middle part of the pavements is more compacted.
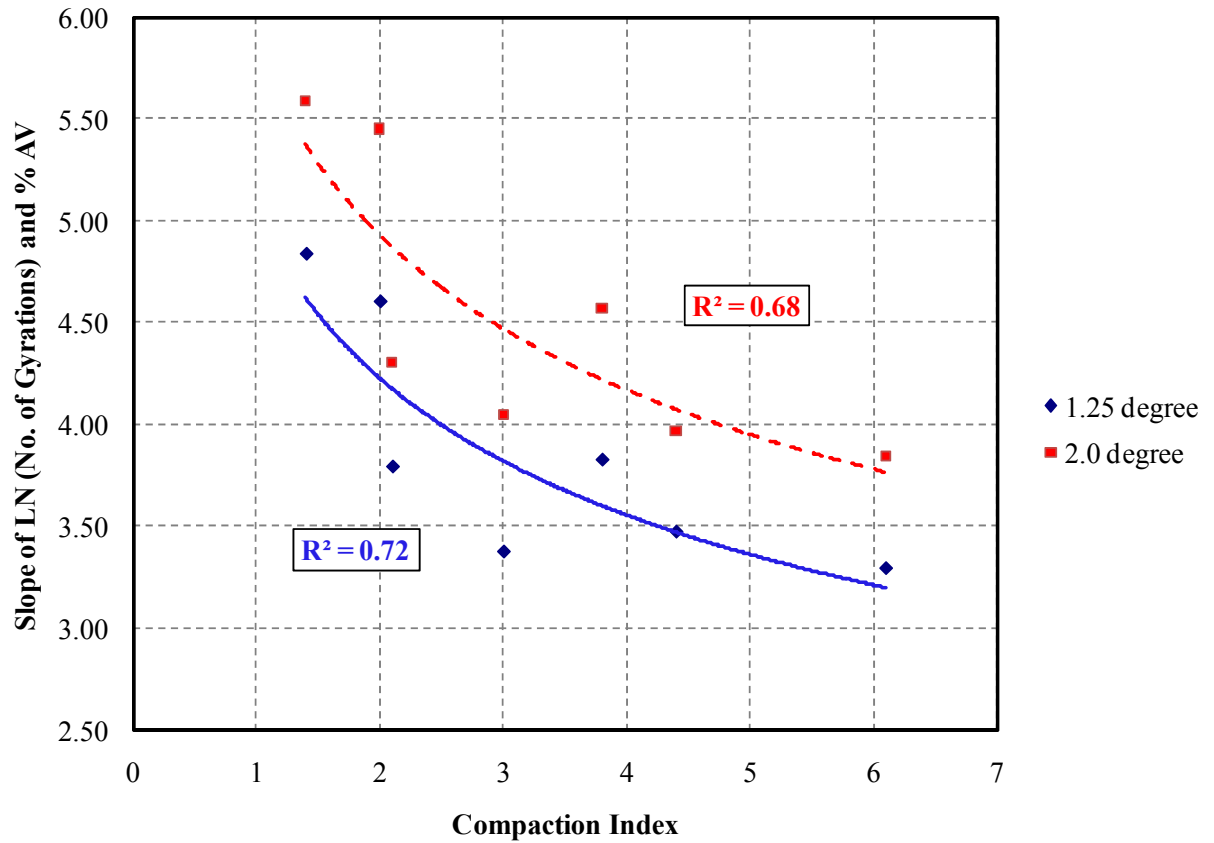
Figure 2-14. Compaction Index versus the Slope of LN (No. of Gyrations) and Percent Air Voids Curve at 8 Percent Air Voids for Different Mixes.
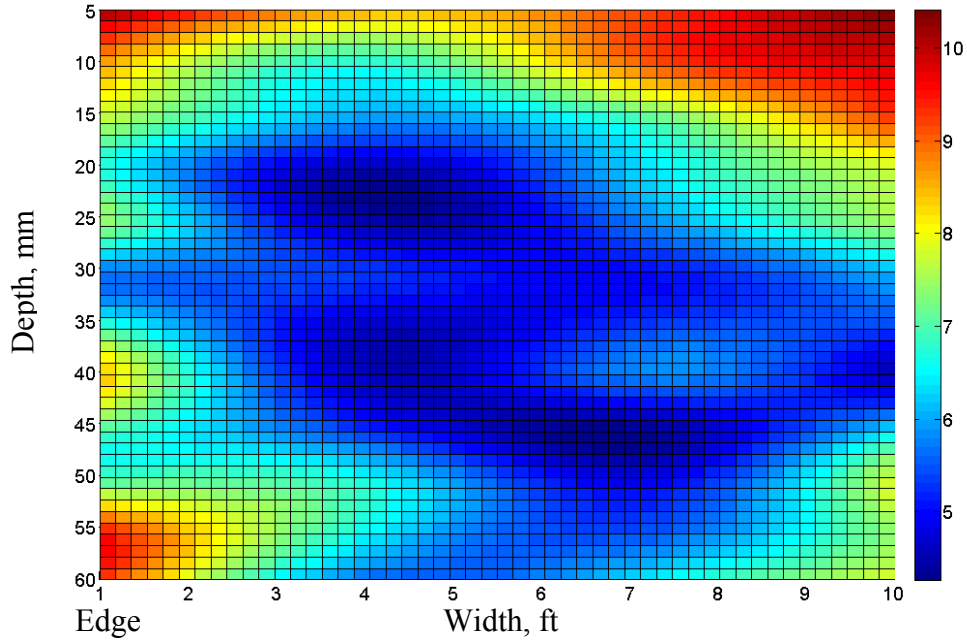
Note: the Total Width of the Mat is 11 ft.

Figure 2-15. Air Void Distribution (%) along the Depth of the Mat for SH 6 Test Section.
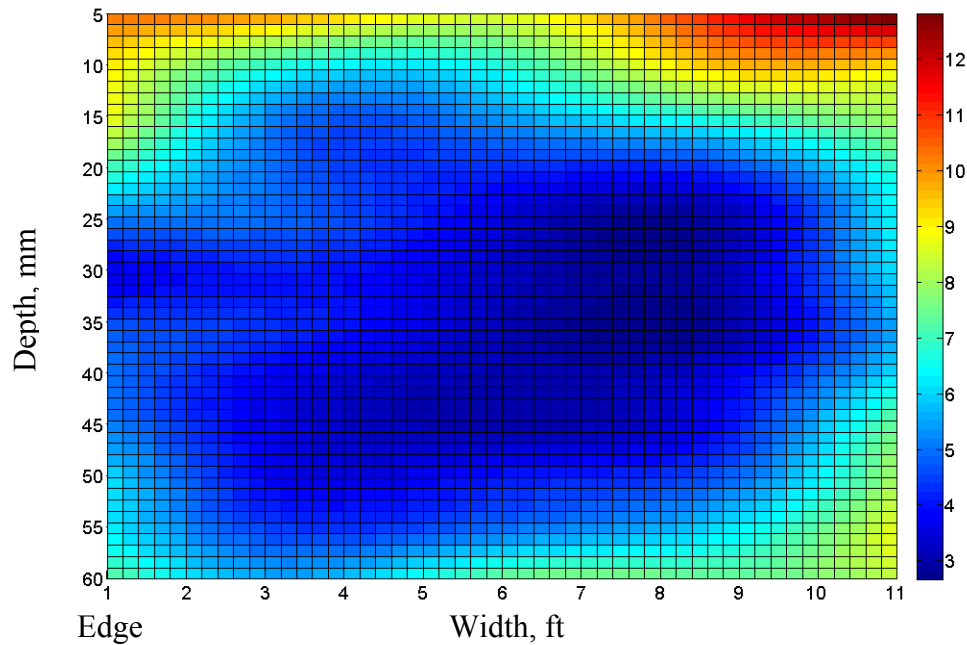
Note: the Total Width of the Mat is 12 ft.

Figure 2-16. Air Void Distribution (%) along the Depth of the Mat for SH 44 Test Section.

23
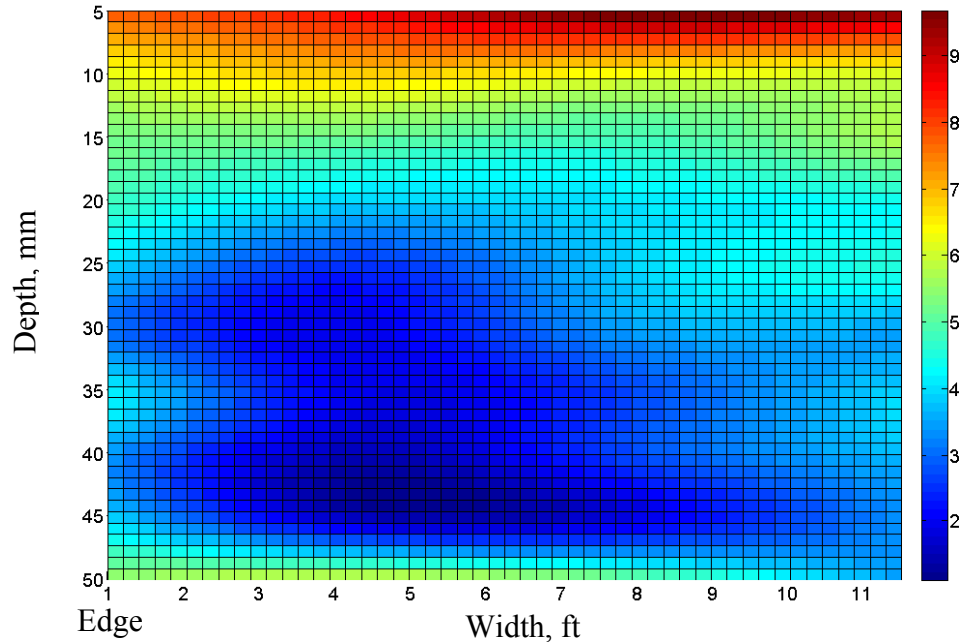
Note: the Total Width of the Mat is 12.5 ft.

Figure 2-17. Air Void Distribution (%) along the Depth of the Mat for SL 1 Test Section.

Comparison of Laboratory and Field Mechanical Properties

The research team obtained field cores from the test sections. These cores were tested to measure density, air void distribution using X-ray CT, permeability, rutting resistance using a Hamburg wheel tracking device, and fatigue resistance using an overlay tester. In addition, laboratory specimens were prepared using virgin materials obtained from the HMA plants for the test projects. These tests procedures were discussed in detail in Report 0-5261-1. Table 2-3 summarizes the results with the specimens obtained from the last three field projects.

Table 2-3. Summary of Mechanical Tests Results.

	Permeability Test, cm/sec		Overlay Test, # of Cycles		Hamburg Test, Rutting Rate	
	Field	Lab.	Field	Lab.	Field	Lab.
HW 6	$1.0x10^{-3}$	$1.0x10^{-3}$	900+	642	2.79	0.79
SH 44	$5.83x10^{-4}$	$5.82x10^{-4}$	88	105	0.55	0.49
SL 1	$8.5x10^{-4}$	$1.3x10^{-3}$	900+	22	2.32	0.75

EFFECT OF THE AIR VOID DISTRIBUTION ON THE HAMBURG TEST

In Report 0-5261-1, the effect of air void distribution on the overlay test results was evaluated. In this section, the effect of the air void distribution on the Hamburg test results was evaluated. The Hamburg results were found to be influenced by the average percent air void (Masad et al. 2008); however the effect of the air void distribution on the Hamburg results was not easy to be evaluated for the following reasons:

- The field cores have a dissimilar percent of air voids which make it difficult to correlate the Hamburg results with the air void structure without considering the effect of the percent of air voids.
- The field cores, which have similar percent air voids, did not have the similar air void distribution in all the projects in this study.

For the previous two reasons, it was difficult to acquire a comprehensive conclusion for all the projects. In order to overcome this problem, a side study was initiated to eliminate the dissimilarity of the percent of the air voids and the average air void distribution. This study included testing a number of laboratory samples fabricated in such a way to induce different air void distributions along the height of the samples. These samples had 7 percent air voids ± 0.50 percent air voids. The US 259 mix, described in Report 0-5261-1, was used in this study as it has experienced a considerable amount of the rutting.

Initially, SGC samples (4-inch height and 6-inch diameter) were prepared. X-ray CT was used to capture the air void distribution along the height of the samples. The samples were cut at specific locations into 2.5-inch samples to induce different air void distributions along the height of the samples; however, they had comparable average percent air void (7±0.5 percent). Four cases were considered. Three cases (2.5-inch height) were cut from long samples (4-inch height) and one case (Case 4) was compacted at 2.5 inches directly such as the conventional way. The average percent air voids in the top part, bottom part, and whole sample are shown in Figure 2-18. Case 1 had relatively higher percent air voids at the top than the bottom part, while Case 2 has less percent air voids at the top than the bottom. Case 3 had equal percent air voids at the top and the bottom part. Case 4, which was compacted directly to 2.5-inch samples, had higher percent air voids at the top than the bottom but with less degree compared to Case 1. The Hamburg results are shown in Figure 2-19 for each case. It can seen that there is no significant difference in the rutting results from one case to another, since all the test samples passed the TxDOT criteria (the rutting is less than 12.5 mm after 20,000 cycles). It can be concluded that unlike the overlay tester, the Hamburg test is less sensitive to the air void distribution within the test samples and is more influenced by the average percent air voids within the test samples.
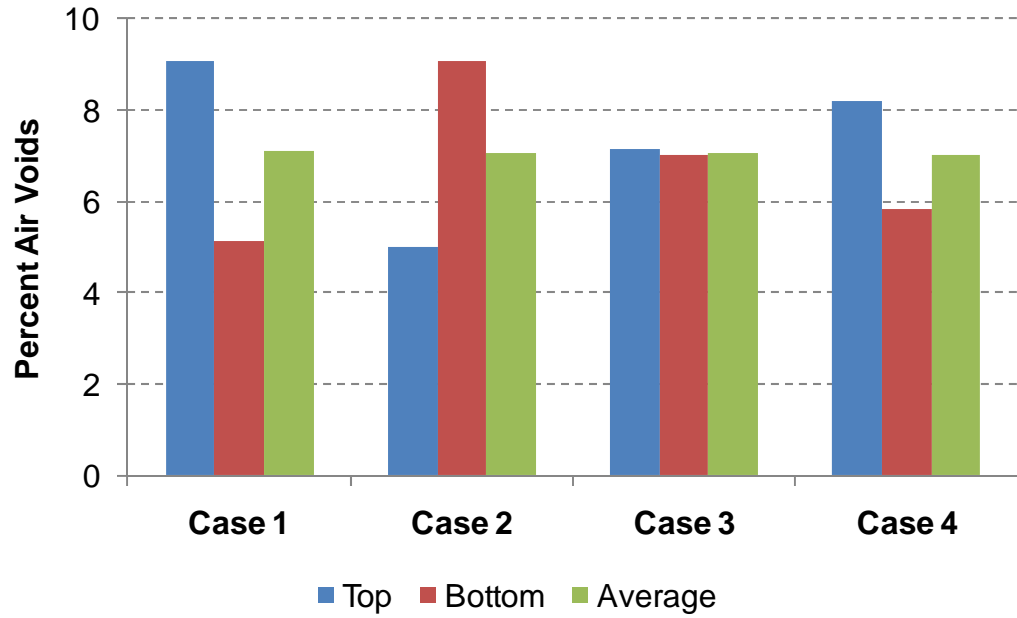
Figure 2-18. The Average, Top, and Bottom Percent of Air Voids for Different Cases.
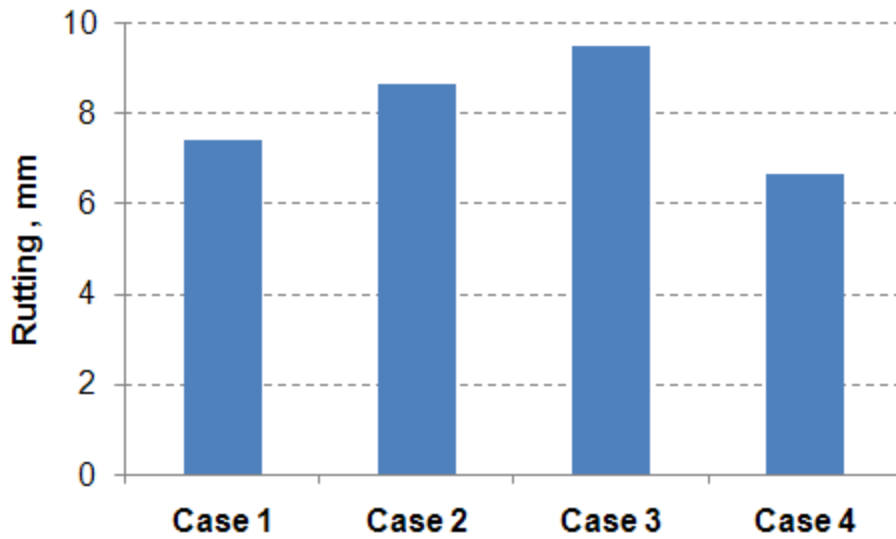
Figure 2-19. Hamburg Test Results for Different Cases.

CONCLUSIONS

       The results of the three test sections evaluated in this part of the project agreed with the findings from Report 0-5261-1. The percent of air voids correlated well with the compaction effort across the mat. The compaction effort was found to be a function of the number of roller passes and the location of each pass across the mat. The efficiency of compaction at a given point is a function of the location of this point with respect to the roller width. A new index, referred to as the Compaction Index, is proposed to quantify the compaction effort at any point in the pavement. The CI is used to study the compactability of asphalt mixtures in the field. The CI correlated well with the slope of the laboratory compaction curves. Asphalt mixtures with higher slope in laboratory needed less CI in the field to achieve the same percent air void. In addition, it was found that in most of the test sections the middle part (across the depth) of the mat is more compacted than the top and bottom parts.

CHAPTER 3

FRACTURE-BASED ANALYSIS OF INFLUENCE OF AIR VOIDS ON MOISTURE DAMAGE

INTRODUCTION AND OBJECTIVES

As discussed in Report 0-5261-1, percent and size of air voids is an important factor that influences asphalt pavement performance. In this chapter, experimental methods and a fracture mechanics approach that accounts for fundamental material properties are used to evaluate the resistance of asphalt mixtures with different percent air voids to moisture damage. Asphalt mixture specimens with different percent air voids were prepared. Test specimens were subjected to dynamic loading under two different conditions: dry (unconditioned) and wet (moisture-conditioned). The moisture conditioning was conducted such that specimens with different percent air voids had the same amount of moisture by varying the moisture conditioning time.

The crack growth index developed originally by Lytton (1993) and later modified and implemented by Masad et al. (2006b) and Arambula (2007) was employed in order to assess resistance to moisture damage. The inputs of the fracture model include the viscoelastic properties, pseudostrain dissipated energy, tensile strength, and the adhesive bond surface energy of asphalt mixture.

ASPHALT MIXTURES TEST SPECIMENS

This mixture was used in the construction of the overlay of the SH 87 in the Yoakum District. The mixture was Type C (TxDOT 1993 Specifications) and designed with Fordyce Gravel and Colorado Materials limestone screening with a PG 76-22 binder. The aggregate gradation is given in Table 3-1 and shown in Figure 3-1.

The Superpave gyratory compactor was used to compact laboratory cylindrical asphalt mixture specimens. The specimens were prepared according to AASHTO standards (2002b). The mixing and compaction temperatures were determined according to TxDOT 2005 specifications based on the binder grade. The mixing and compaction temperature for the PG 76-22s binder are 325°F and 300°F, respectively. The laboratory SGC specimens were 7 inches in height and 6 inches in diameter. The test specimens

were cored from the SGC specimens and trimmed from the top and the bottom to the size of 6 inches in height and 4 inches in diameter. A total of 30 asphalt mixture specimens were compacted such that the final percent air voids after cutting and trimming were 4±0.5, 7±0.5, or 10±0.5 percent.

Table 3-1. Aggregate Gradation of SH 87 Type C Asphalt Mixtures.

	Type C		Type D/F		Man Sand		Field Sand		Limestone		Lime		Combined
Individual %	18		46		10		15		10		1		100
Sieve Size: (mm)	Pass %	Total %	Pass %	Total %	Pass %	Total %	Pass %	Total %	Pass %	Total %	Pass %	Total %	Total %
22.4	100	18	100	46	100	10	100	15	100	10	100	1	100
16	99.5	17.9	100	46	100	10	100	15	100	10	100	1	99.9
9.5	8.3	1.5	97.1	44.7	100	10	100	15	100	10	100	1	82.2
4.75	0.1	0	49.1	22.6	99.8	10	100	15	99.7	10	100	1	58.6
2	0	0	11.2	5.2	97.2	9.7	98.9	14.8	88.1	8.8	100	1	39.5
0.425	0	0	2	0.9	35.7	3.6	46.2	6.9	44.2	4.4	100	1	16.8
0.18	0	0	1	0.5	11	1.1	5.3	0.8	32.1	3.2	100	1	6.6
0.075	0	0	0.5	0.2	2.2	0.2	0.5	0.1	24.6	2.5	99	1	4
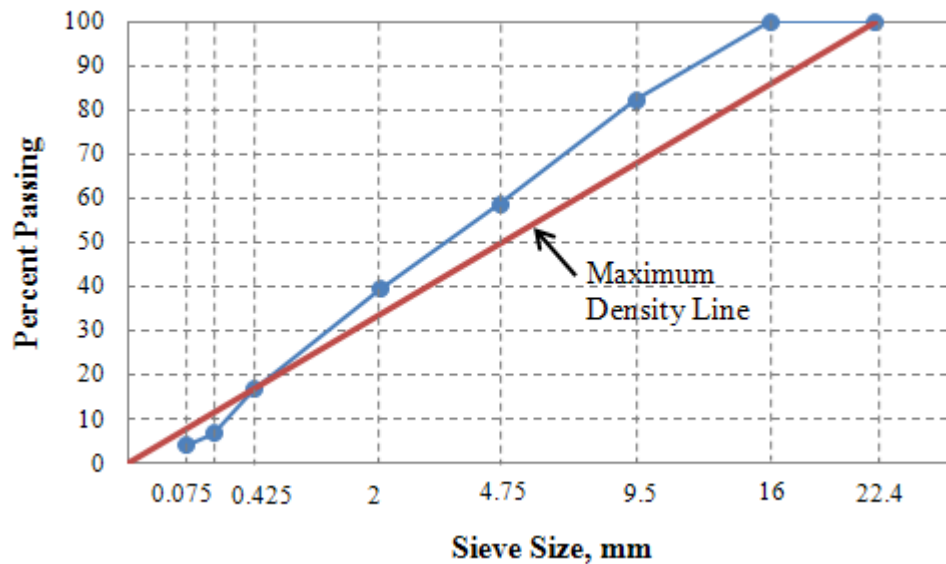
Figure 3-1. 0.45 Power Aggregate Gradation Chart.

MOISTURE CONDITIONING

Half of the test specimens (five specimens at each percent air voids) were subjected to moisture conditioning following the modified Lottman procedure without the freezing stage (AASHTO 2007). A vacuum of 3.38 kPa absolute pressure (736.6 mm Hg. partial pressure) was used in this study for moisture conditioning. Several specimens at different percent air voids were prepared and conditioned for different times in order to determine the time needed to achieve the required saturation level between 70 to 80 percent as required by AASHTO T-283-07. The time measurement started once a vacuum of 3.38 kPa absolute pressure was achieved. Table 3-2 presents the time required to achieve the target saturation level for specimens with different percent air voids. This procedure was followed by placing specimens in a 60 °C water bath for 24 hours. Then, the test specimens were taken to another 20 °C water bath to cool down before testing.

Table 3-2. Vacuum Saturation Time.

Percent Air Voids	Time, Sec
4	90
7	45
10	25

EXPERIMENTAL TESTS

The following section will cover the experimental tests by which the model's inputs were determined.

Relaxation Test

This test was used to determine the viscoelastic properties which include the initial relaxation modulus (E_o) and the modulus relaxation rate (m). A constant axial tension strain of 80 microstrain was applied to the test specimens for 60 sec followed by 600 sec rest period. Then, a constant compression strain of 80 microstrain was applied for 60 sec. The time interval used to increase the load from 0 to a constant value of 80

31

micron was 6 sec. Figure 3-2 shows the applied load. The test was performed at a temperature of 20°C. The test specimens kept at this temperature for 2 hours before testing. The loading was applied by using an Mechanical Testing System (MTS) where the data (time, load, and deformation) were recorded. The deformation was measured by Linear Variable Differential Transformers (LVDTs). Six LVDTs were used to measure the deformation; three LVDTs were used to measure the axial deformation and the other three were used to measure the radial deformation. The LVDTs were placed at 120° along the circumference of the test sample, and three radial LVDTs were placed at the middle of the test specimens. Figures 3-3 and 3-4 show the LVDTs configuration. The gauge length between the axial LVDT holders was 4 inches.

The time-dependent relaxation modulus is calculated according to Equation 3-1.
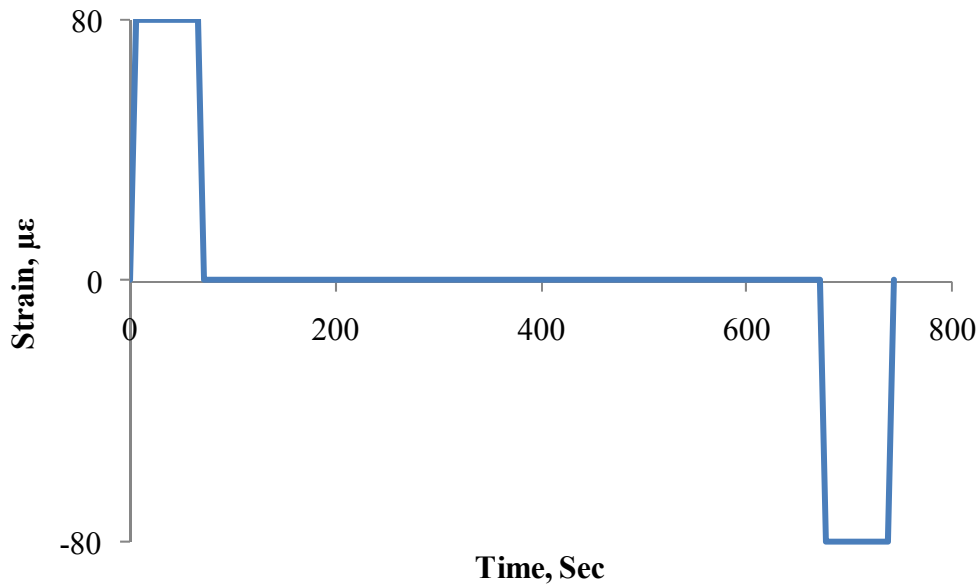
Figure 3-2. Applied Load during the Relaxation Test.

$$E(t) = \frac{P(t)}{\pi r^2 \varepsilon} \qquad\qquad 3\text{-}1$$

where: $E(t)$ = time-dependent relaxation modulus, $P(t)$ = measured load, r = specimen radius, ε = applied strain.

A power law equation was fitted to the test data to determine the viscoelastic parameter as described in Equation 3-2.

$$E(t) = E_o t^{-m} \qquad \text{3-2}$$

where E_o = the initial relaxation modulus and m = the modulus relaxation rate.
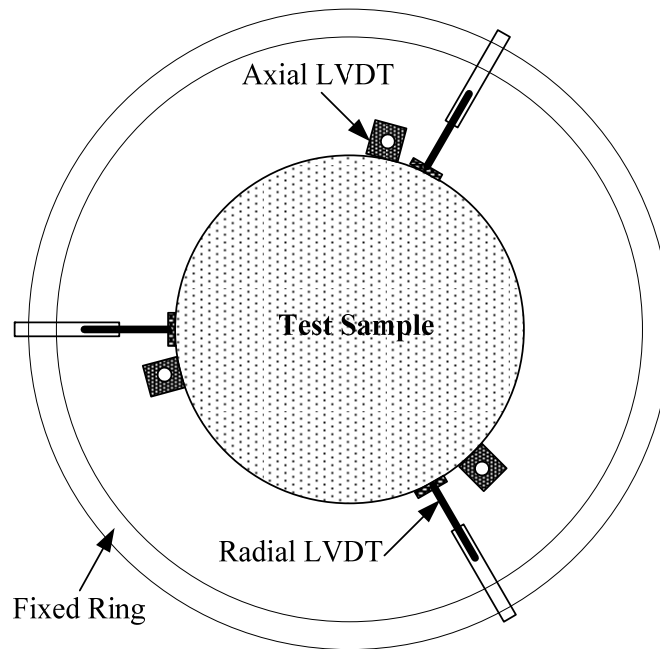
Figure 3-3. Schematic View of LVDTs Configurations.
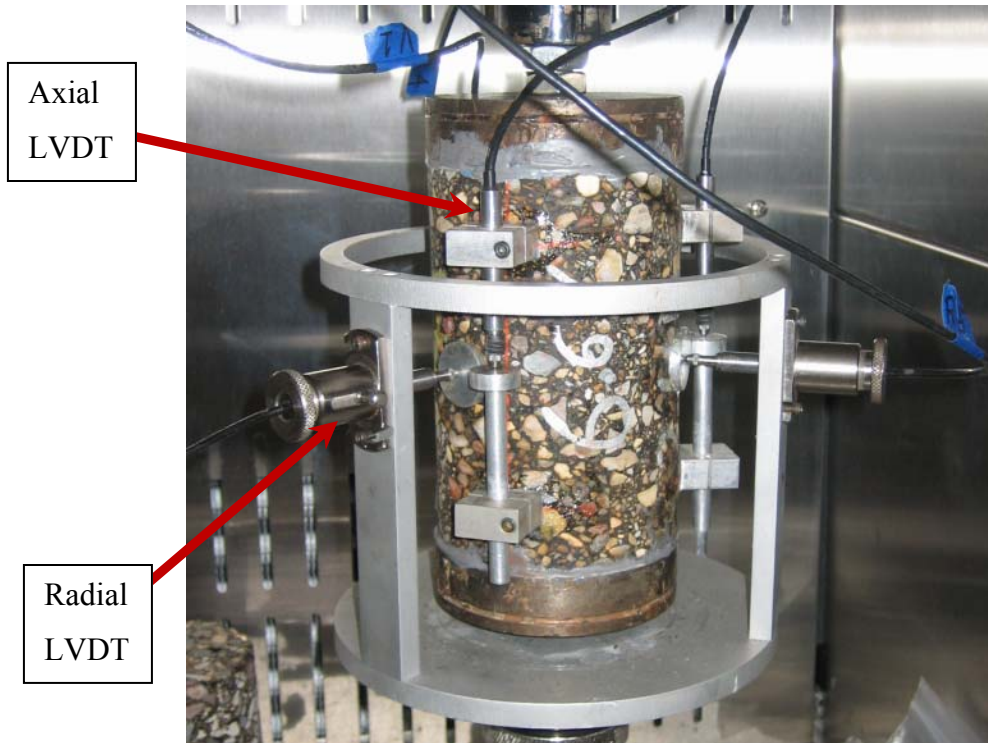
Figure 3-4. LVDTs Configuration.

Dynamic Direct Tension Test

The dynamic direct tension test applied a haversine strain shape with a maximum of 140 microstrain for 0.1 sec followed by a rest period of 0.9 sec, as shown in Figure 3-5. A total number of 1000 loading cycles were applied on each specimen. The haversine strain waveform simulates the shape of field pulse developed under moving wheel loads of the commercial vehicles on the highways (Si 2001).

Several criteria were established to select the strain level for the dynamic direct tension test. The strain level should be high enough to induce cumulative fatigue damage in all specimens with different percent air voids without failing the test specimens. As discussed later, damage is quantified by the area of the stress-pseudostrain hysteresis loop. From previous experience, we know that test variability and problems in measuring devices increases significantly when specimens start to show disintegration and are close to the failure point. Different strain levels were evaluated, and 140 microstrain was found to meet the test criteria. The data were recorded every 50 cycles. The recorded data

points within a single loading cycle should be sufficient to study the dissipated pseudostrain energy. In this test, for every single recorded loading cycle, the data were captured every 0.005 sec. The LVDTs configurations were the exact same used in the relaxation modulus test. The test was conducted at a constant temperature of $20^{\circ}C$. Test specimens were conditioned at this temperature for about two hours before conducting the test.
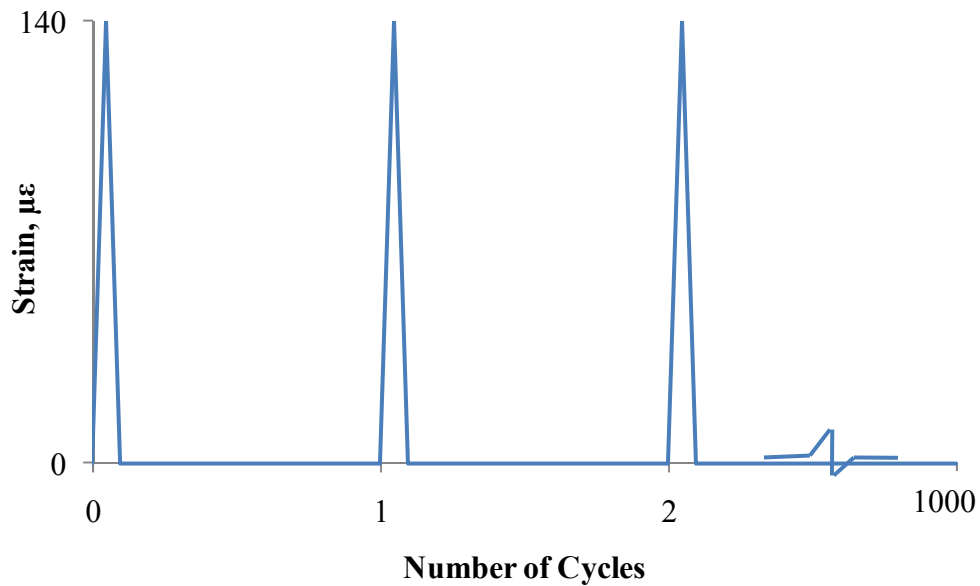
Figure 3-5 Applied Loading Configurations for Dynamic Direct Tension Test.

The viscoelastic stress (σ_V) was computed using the Boltzman superposition for every loading cycle as follows (Arambula 2007):

$$\sigma_V(\tau_k) = \sum_{i=1}^{k} E_o(\tau_k - t_i)^{-m} C_i dt \qquad \text{3-3}$$

where: E_o = initial relaxation modulus determined using the relaxation test, τ_k and t_i = the present and previous time, m = the modulus relaxation rate determined using the relaxation test, $C_i = (d\varepsilon/dt)$ the change in strain for every load increment, dt = time increment, k = number of data points.

35

The measured time-dependent tensile stress was calculated in Equation 3-4.

$$\sigma_m(t) = \frac{P(t)}{\pi r^2}$$

3-4

where: $P(t)$ = the measured load, r = the radius of the sample.

The reference modulus (E_R) was estimated according to Equation 3-5.

$$E_R = \frac{\sigma_m(t)\,max}{\varepsilon(t)\,max}$$

3-5

where: $\sigma_m(t)max$ = the maximum measured time-dependent tensile stress at the first load cycle, $\varepsilon(t)max$ = the maximum measured time-dependent tensile strain at the corresponding cycle.

The pseudostrain (ε_R) is the ratio between the viscoelastic stress (σ_V) and the reference modulus (E_R) as given in Equation 3-6.

$$\varepsilon_R(t) = \frac{\sigma_V(t)}{E_R}$$

3-6

The dissipated pseudostrain energy (DPSE) is the area of hysteresis loop of the measured tensile stress $\sigma_m(t)$ against the calculated pseudostrain (ε_R) as shown in Figure 3-6. The area was computed using the double meridian distance method (Wolf and Ghilani 2002). To account for the reduction in the matter that is able to dissipate the energy, the DPSE was normalized by the ratio of (PS_i/PS_o) as follows:

$$W_R = \frac{DPSE}{(PS_i\,/\,PS_o)}$$

3-7

where, W_R= normalized DPSE, PS_i = pseudostiffness at each load cycle, and PS_o = the maximum pseudostiffness at the first load cycle. The pseudostiffness is the ratio of maximum measured stress to maximum computed pseudostrain. The normalized DPSE quantifies the real damage during the dynamic direct tension test.

The relationship between the normalized DPSE (W_R) and the number of load cycles is presented in a semi-log graph in Figure 3-7. This relationship yields a trend line which has the following form:

$$W_R = a + b\ln(N)$$

3-8

where, b = the rate of fracture damage accumulation, a = the energy associated with the initial damage which corresponds to the first load cycle.
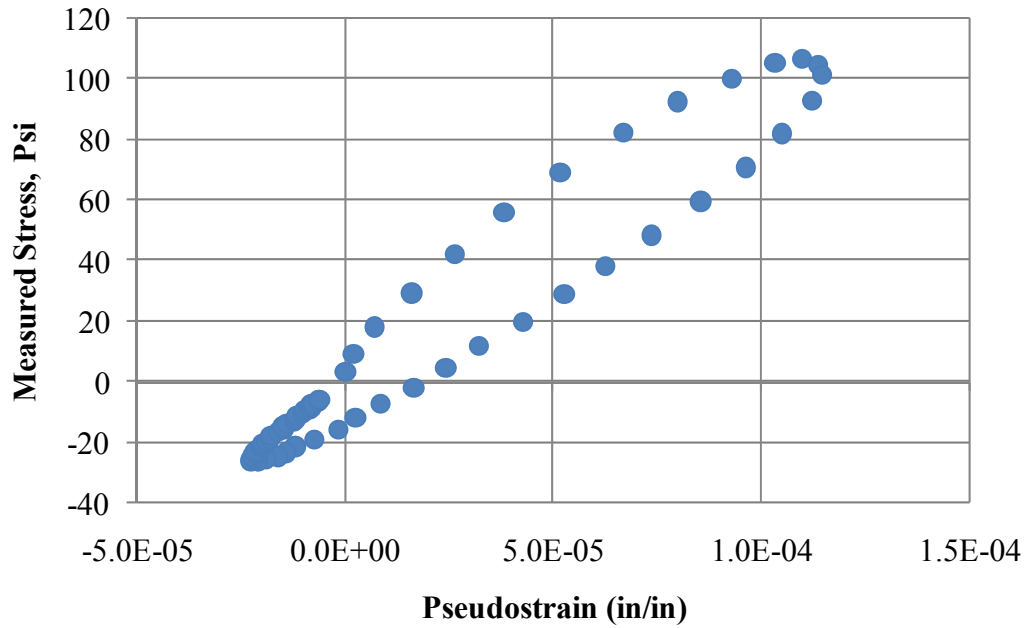
Figure 3-6 An Example of Measured Stress vs. Pseudostrain.
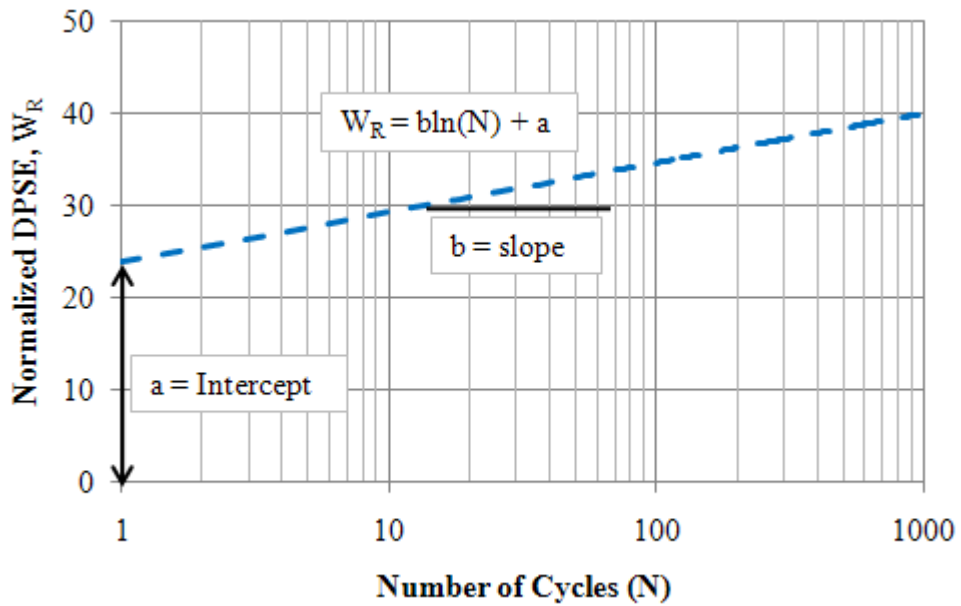
Figure 3-7. Normalized DPSE, W$_R$ vs. Number of Cycles.

Tensile Strength Test

This test was used to determine the tensile strength of the test specimens. The tensile strength is a required input in the fracture model. This test was conducted at 20°C after 10 min of the completion of the dynamic direct tension test. A test sample was continuously pulled at a constant rate of 0.05 inch/min until the failure occurs.

Figure 3-8 shows a test specimen after failure inside the Materials Testing System (MTS), while Figure 3-9 shows the failure for the test specimens in dry and wet conditions. Figure 3-9(a) displays the failure in wet condition where the aggregates were stripped from the binder. Figure 3-9(b) shows the failure in dry condition where the aggregates were still coated very well with the binder.

Figure 3-8. Test Sample after Failure inside the MTS.

<div align="center">(a)   (b)</div>

Figure 3-9. Test Specimens after Failure (a) Wet Condition, (b) Dry Condition.

Surface Energy Measurements

The surface energy was used to estimate the adhesive bond surface energy between asphalt binder and aggregate and the cohesive bond energy of asphalt binder (Arambula 2007; Howson et al. 2007). The surface energy can be defined as the required work to create a unit surface area. The surface free energy has three separate components (Howson et al. 2007): monopolar acidic (Γ^+,), monopolar basic (Γ^-) and apolar or Lifshitz-van der Waals (Γ^{LW}). The total surface free energy is calculated according to Equation 3-9.

$$\Gamma = \Gamma^{LW} + 2\sqrt{\Gamma^+\Gamma^-} \qquad\qquad 3\text{-}9$$

The adhesive bond energy (ΔG_f) is a required parameter in the proposed model. The Wilhelmy plate (WP) test and the Universal sorption device (USD) are used to determine the surface energy components of asphalt binder and aggregates, respectively. Table 3-3 presents the surface energy components for the asphalt binder and aggregates.

The adhesive bond energy between the binder (subscript A) and aggregate (subscript S) was calculated using Equation 3-10. The adhesive bond energy when the water (subscript W) displaces asphalt binder from its interface with the aggregate is presented in Equation 3-11.

$$\Delta G_{AS}^a = 2\sqrt{\Gamma_A^{LW}\Gamma_S^{LW}} + 2\sqrt{\Gamma_A^+\Gamma_S^-} + 2\sqrt{\Gamma_A^-\Gamma_S^+} \qquad\qquad 3\text{-}10$$

$$\Delta G_{ASW}^{wet} = \Gamma_{AW} + \Gamma_{SW} - \Gamma_{AS} \qquad\qquad 3\text{-}11$$

Equation 3-12 represents the energy of the interface between any two materials (*i* and *j*).

$$\Gamma_{ij} = \Gamma_i + \Gamma_j - 2\sqrt{\Gamma_i^{LW}\Gamma_j^{LW}} - 2\sqrt{\Gamma_i^+\Gamma_j^-} - 2\sqrt{\Gamma_i^-\Gamma_j^+}$$

3-12

The energy ratio (ER), which was reported by Howson et al. 2007, is presented in Table 3-3 for this particular combination of binder and aggregates.

Table 3-3. Surface Energy Components.

Materials	Wetting or Dewetting	Γ	Γ^{LW}	Γ^+	Γ^-	ER
Asphalt Binder (PG 76-22)	Wetting	22.03	21.36	0.05	2.12	0.19
	Dewetting	43.56	43.56	0.00	13.11	0.05
Aggregates	N/A	111.34	44.37	1.63	687.89	N/A
Water	N/A	72.80	21.80	25.50	25.50	

CRACK GROWTH FRACTURE MODEL

A crack growth index was used to evaluate the performance and moisture sensitivity of asphalt mixtures. The crack growth index was developed originally by Lytton (1993) and later modified by Masad et al. (2006b) and Arambula (2007). Herein, the crack growth index was employed in order to assess the resistance to moisture damage of asphalt mixtures with different percent air voids. This section includes a brief description of the crack growth model, and the reader is referred to Arambula (2007) for more details and the complete derivation. The crack growth was derived from Paris's law (Equation 3-13).

$$\frac{dr}{dN} = A(J_R)^n$$

3-13

where: r = average crack radius, N = number of load cycles, A and n = material constants, and J_R = J-integral or the change in pseudostrain energy per unit volume to the change in crack surface area.

$$J_R = \cfrac{\cfrac{\partial W_R}{\partial N}}{\cfrac{\partial (c.s.a)}{\partial N}} \qquad\qquad 3\text{-}14$$

where: W_R = DPSE per unit volume, $c.s.a$ = crack surface area. The equation used to estimate the crack growth parameter (r) is presented in Equation 3-15 (Arambula (2007).

$$r = \left[r_o^{\frac{2n+1}{1+n}} + (2n+1)\left(\frac{bE_R}{4\pi E_1 \Delta G_f \sigma_t^2}\right)^{\frac{n}{1+n}} \left(N^{\frac{1}{1+n}} - 1^{\frac{1}{1+n}} \right) \right]^{\frac{1+n}{2n+1}} \qquad 3\text{-}15$$

The initial damage is caused by the presence of initial cracks and voids (r_o). Due to the materials nonlinearity at higher strain levels, it is difficult to separate the initial energy into nonlinear and initial damage fractions. Consequently, the initial energy was subtracted from the pseudostrain energy. Test specimens were compared based on the crack growth behavior, which is represented by the second part of Equation 3-15. The crack growth index (CGI) is presented in Equation 3-16 (Arambula 2007).

$$CGI = \left[(2n+1)^{\frac{1+n}{2n+1}} \left(\frac{bE_R}{4\pi E_1 \Delta G_f \sigma_t^2}\right)^{\frac{n}{2n+1}} \left(N^{\frac{1}{1+n}} - 1^{\frac{1}{1+n}} \right)^{\frac{1+n}{2n+1}} \right] \qquad 3\text{-}16$$

where: CGI = crack growth index, N = number of load cycles, n = material constant equals to reciprocal of the modulus relaxation rate (m), E_o= initial relaxation modulus, ΔG_f= adhesive bond surface energy between asphalt binder and aggregate, σ_t= tensile strength, E_R= reference modulus, $b = \partial WR / \partial \ln(N)$, W_R= pseudostrain energy per unit volume of the intact material.

EXPERIMENTAL TESTS RESULTS

In the following section the results of the experimental tests will be presented and discussed.

Results of Tensile Relaxation Test

Figure 3-10 shows the change of the tensile relaxation modulus over time for tested specimens at different percent air voids. Figure 3-11 shows the ratio of the initial tensile relaxation modulus in wet condition to the one in dry condition. The results show

that the tensile relaxation modulus decreased with the increase in percent air voids. In addition, the ratio of tensile relaxation modulus in wet condition to the one in dry condition decreased with an increase in percent air voids. It is interesting to note from Figure 3-10 that the percent air voids cause a shift in the relaxation modulus curve. This indicates that a relaxation modulus-percent air voids shift function can be introduced to predict the change in modulus with changes in air voids.
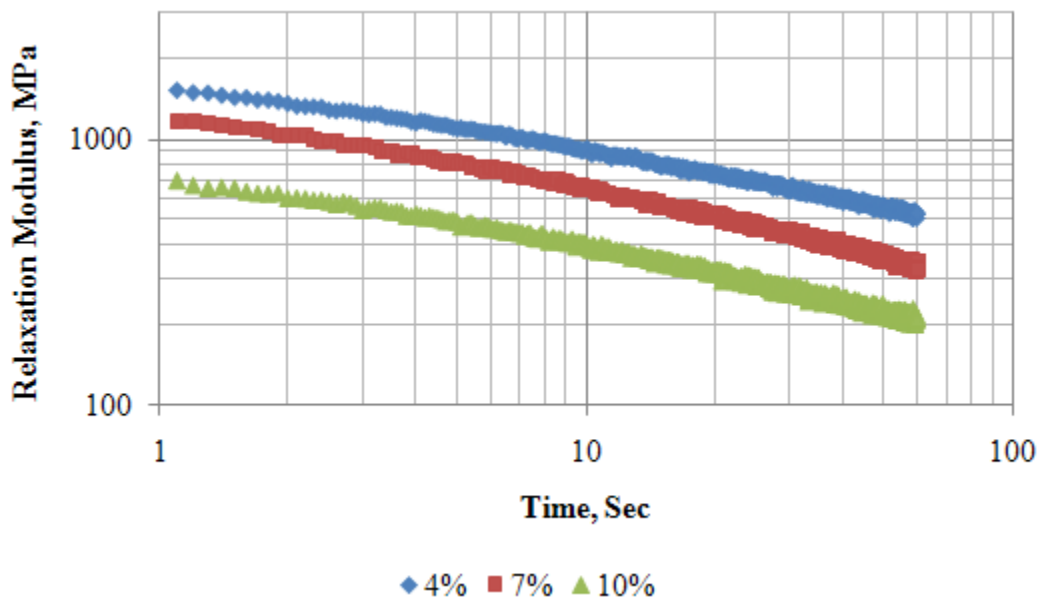
Figure 3-10. Examples of Tensile Relaxation Test Results at Different Percent Air Voids in Dry Conditions.

Results of Dynamic Direct Tension Test

Figure 3-12 shows the change of the normalized DPSE (W_R) with the load cycles for tested specimens at different percent air voids. Figures 3-13 and 3-14 show the average intercept (a) at different percent air voids in dry and wet conditions, respectively. The average slope (b) plotted versus percent air voids in dry and wet conditions is shown in Figures 3-15 and 3-16, respectively. By examining the results, the following observations can be made:
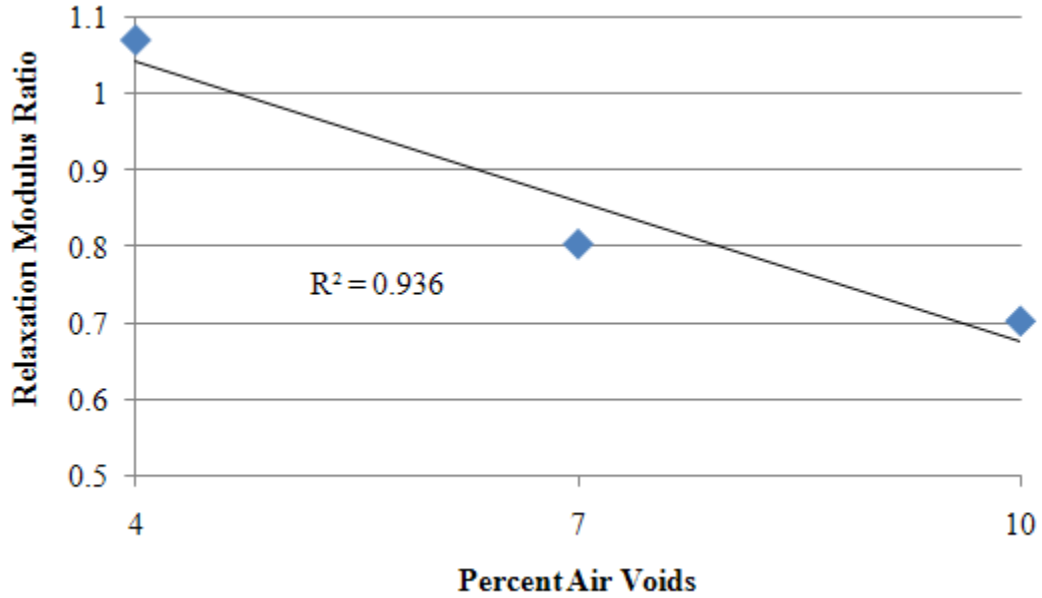
Figure 3-11. Initial Tensile Relaxation Modulus Ratio versus Percent Air Voids.

- The normalized DPSE (W_R) correlated very well with the number of cycles in a semi-log scale.

- The initial W_R or the intercept (a) decreases with the increase in percent air voids.

- The rate of fracture damage accumulation or slope (b) increases with the increase in the initial W_R.
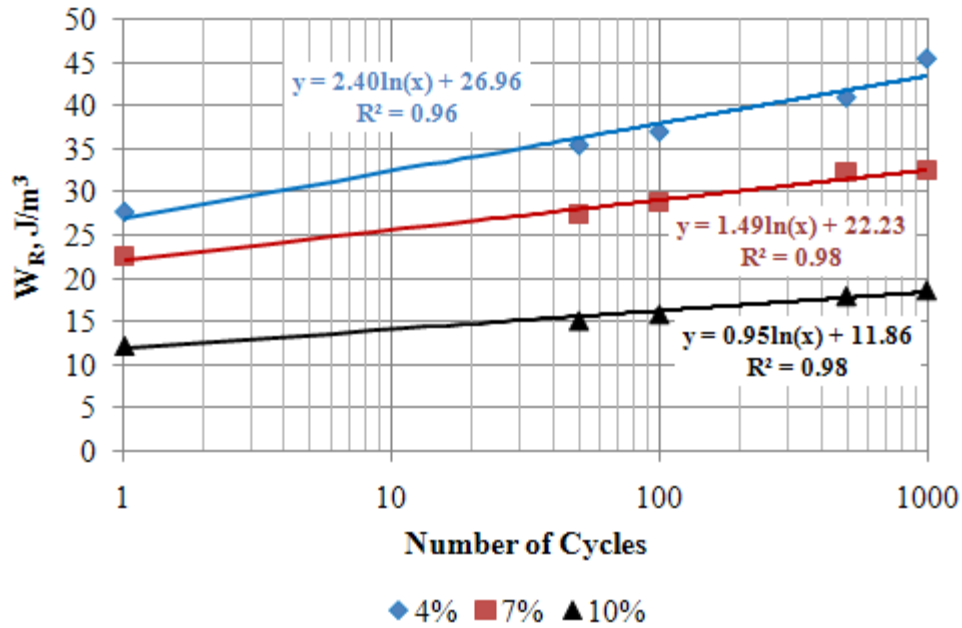
Figure 3-12. Normalized DPSE (W_R) versus Number of Cycles at Different Percent Air Voids.
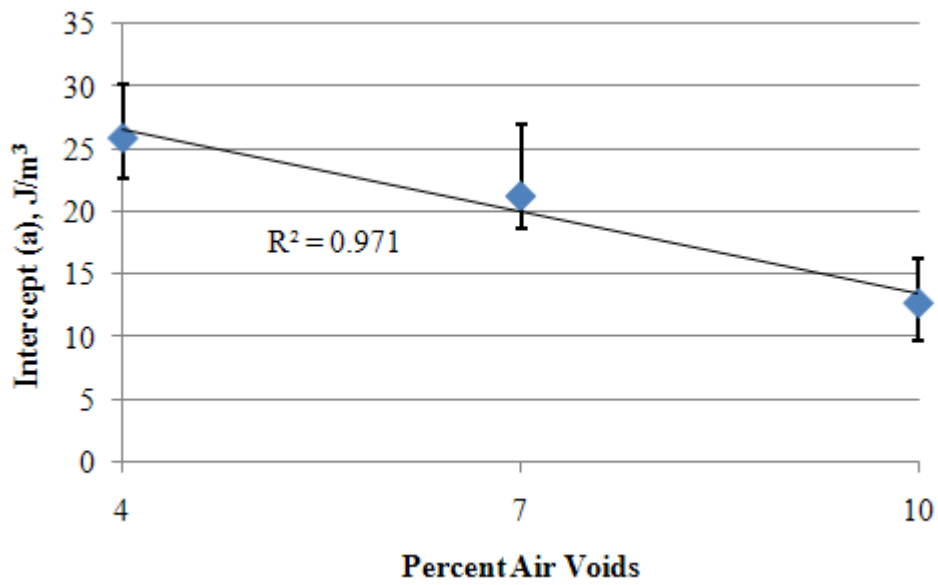
Figure 3-13. Intercept (a) versus Percent Air Voids in Dry Conditions.
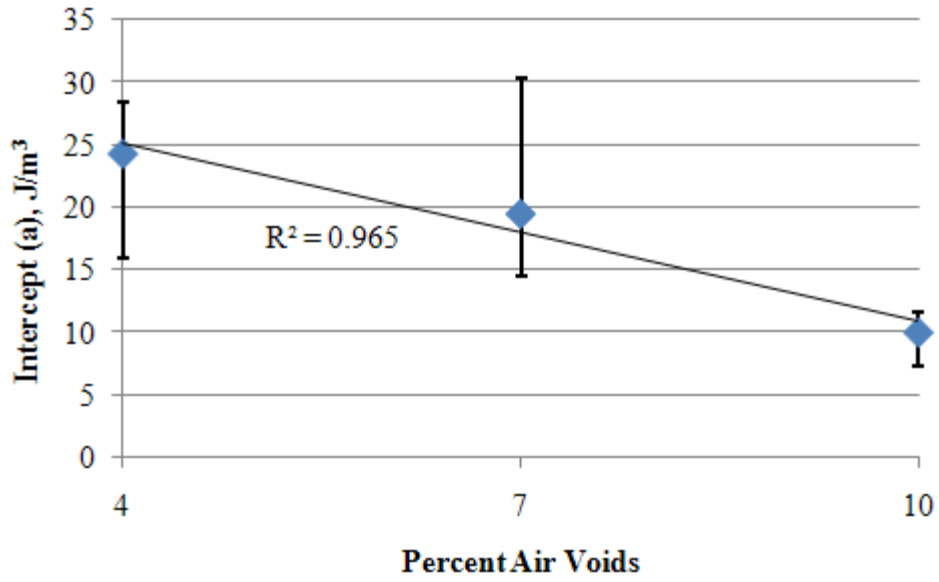
Figure 3-14. Intercept (a) versus Percent Air Voids in Wet Conditions.
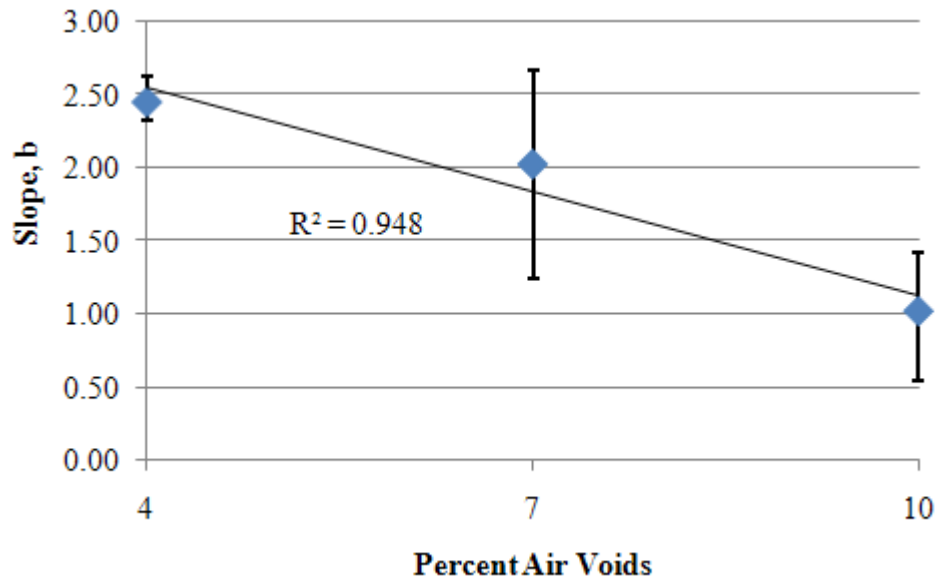
Figure 3-15. Percent Air Voids versus Slope (b) in Dry Conditions.
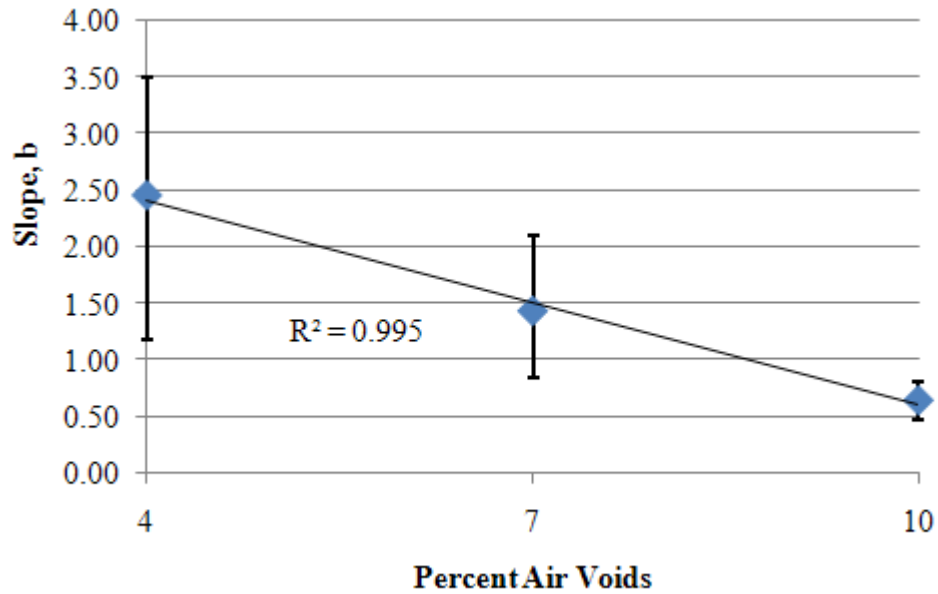
Figure 3-16. Percent Air Voids versus Slope (b) in Wet Conditions.

Results of Tensile Strength Test

Figures 3-17 and 3-18 present the average tensile strength for test specimens with different percent air voids in dry and wet conditions, respectively. The ratio of the average tensile strength in wet condition to the average tensile strength in dry condition at different percent air voids is shown in Figure 3-19. The results show the following:

- The tensile strength decreased with the increase in percent air voids.
- The ratio of tensile strength in wet condition to the one in dry condition decreased with the increase in percent air voids.
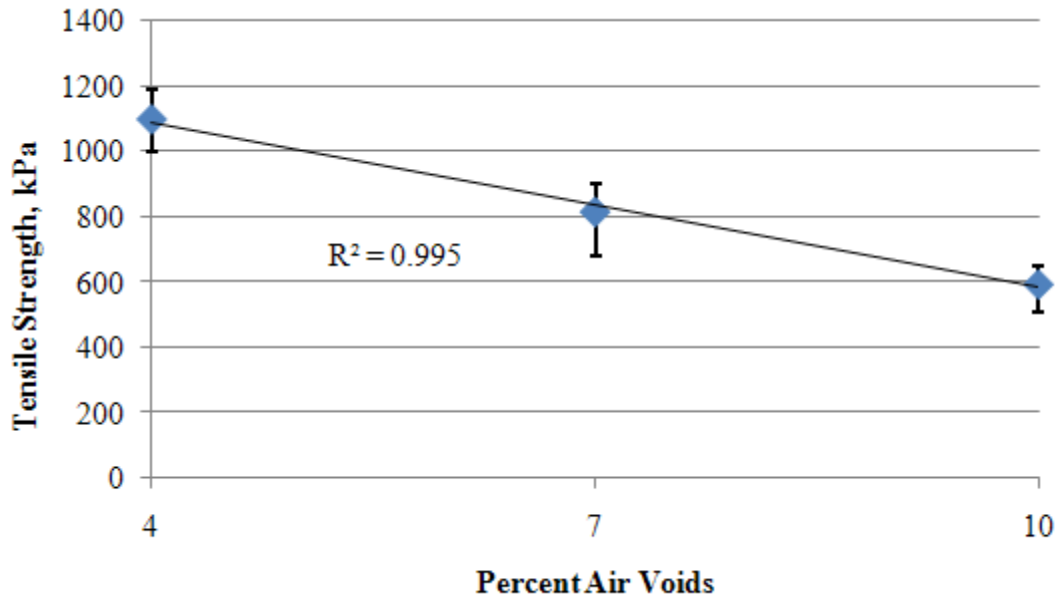
Figure 3-17 Average Tensile Strength versus Percent Air Voids in Dry Conditions.
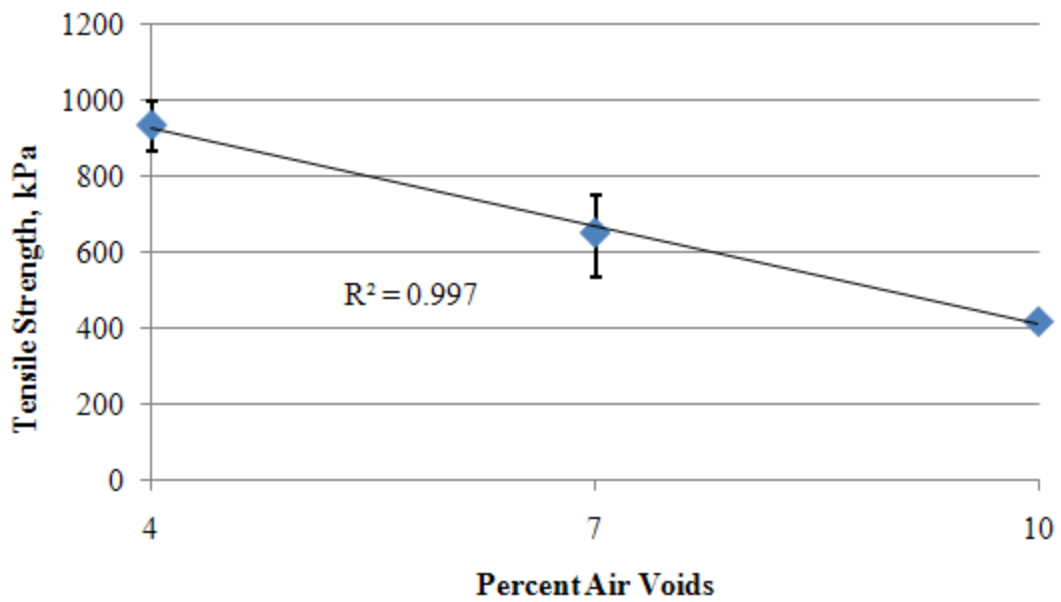
Figure 3-18. Average Tensile Strength versus Percent Air Voids in Wet Conditions.
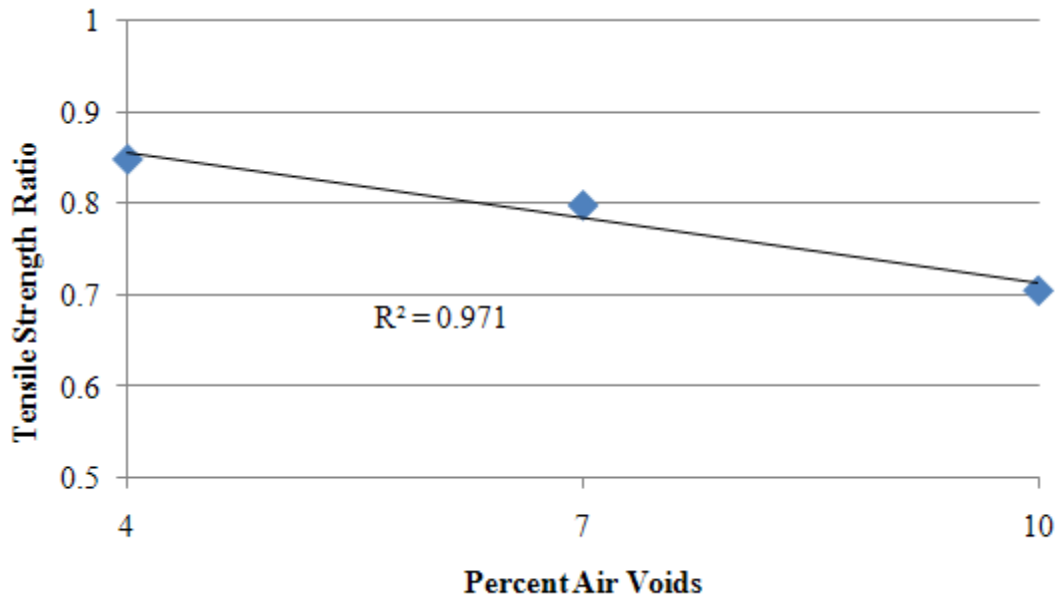
Figure 3-19. Tensile Strength Ratio versus Percent Air Voids.

Results of Adhesive Bond Energy

Surface energy components of the asphalt binder and aggregates given in Table 3-3 were used to determine the adhesive bond energy between asphalt and aggregates. Equations 3-10 and 3-11 were used to calculate the adhesive bond energy between the aggregates and asphalt binder in dry and wet conditions, respectively. The adhesive bond energy of the fracture components in Equation 3-16 was determined to be 97.17 erg/cm^2 in dry condition and -195.41 erg/cm^2 in wet condition. However, the test specimens were not fully saturated of water in the wet conditions. The adhesive bond energy in wet condition was assumed to be proportional to the ratio of the reference modulus in wet condition to the one under the dry condition as given in Equation 3-17.

$$\Delta G_f = \frac{E_R(Wet)}{E_R(Dry)} \Delta G_{AS}^a$$

3-17

Table 3-4 summarizes the required parameters in the crack growth index model.

Table 3-4. Average Parameters for the Fracture Model.

Percent Air Voids	Condition	E_0 Mpa	m	E_R Mpa	a J/m^3	b	σ_t kPa	ΔG_f J/m^2
	Dry	1843.38	0.316	5469.36	25.97	2.45	1100.69	0.09717
4	Wet	1974.2	0.341	5375.76	24.35	2.46	935.17	0.09551
	Dry	1394.34	0.318	4437.34	21.43	2.03	816.55	0.09717
7	Wet	1122.37	0.334	3983.1	19.56	1.44	652.41	0.08722
	Dry	808.05	0.298	4094.03	12.79	1.03	594.48	0.09717
10	Wet	594.38	0.316	3436.79	10.09	0.65	419.31	0.08456

RESULTS AND ANALYSIS

The results show that the relaxation modulus decreased with the increase in percent air voids. Specimens with higher percent air voids accumulate damage at a lower rate than specimens with low percent air voids. This is evidenced in the lower (a) and (b) values at high percent air voids. However, specimens with high percent air voids had lower strength as shown in the tensile strength values reported in Table 3-4. Figure 3-20 shows the crack growth index against (CGI) the number of load cycles for the test specimens. Specimens with less percent air voids had less CGI than the ones with high percent air voids in dry and wet conditions, which means better performance or more resistance to the fracture damage. The dry specimens had less CGI than the wet ones at each percent air voids. The CGI ratio, which is the CGI in wet condition to the one in dry condition, at each percent air voids is shown in Figure 3-21. The CGI ratio at 7 percent air voids was less than the one at 4 and 10 percent air voids. This result means that the detrimental effect of the moisture was minimal at 7 percent air voids. However, it should be pointed out that samples with less percent air voids performed better.
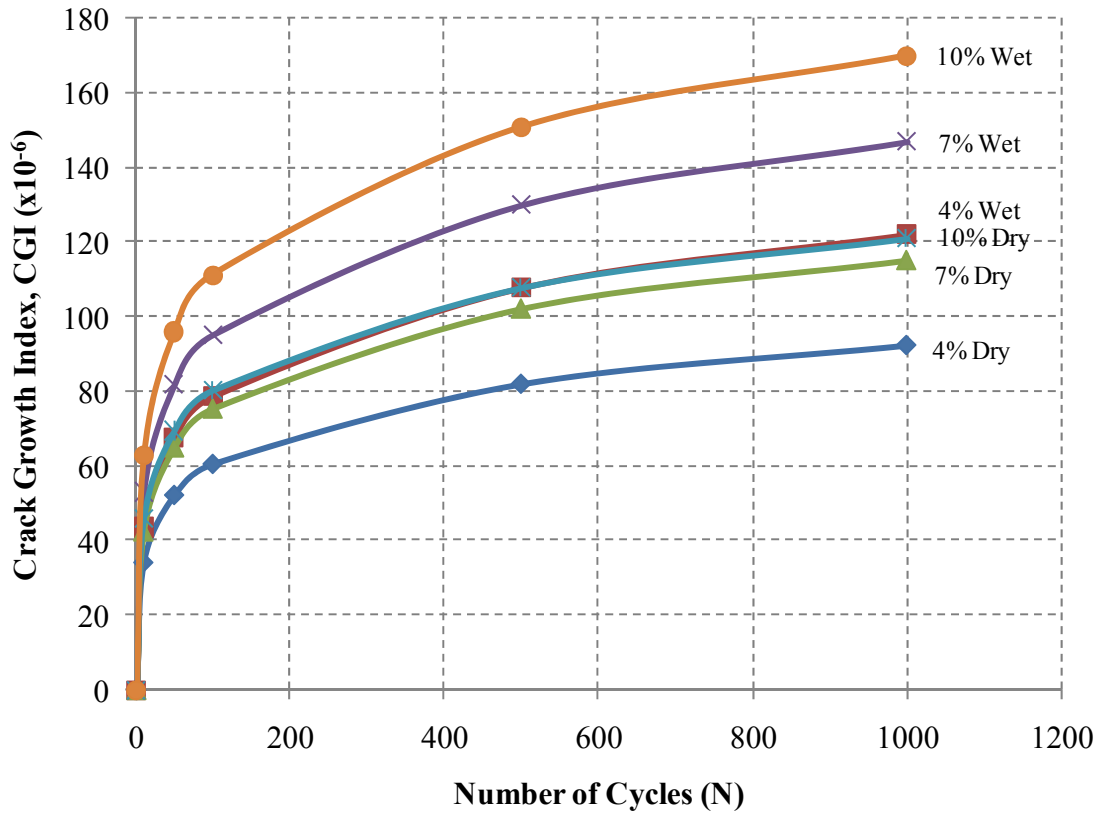
Figure 3-20. Crack Growth Index at Different Percent Air Voids in Dry and Wet Conditions.
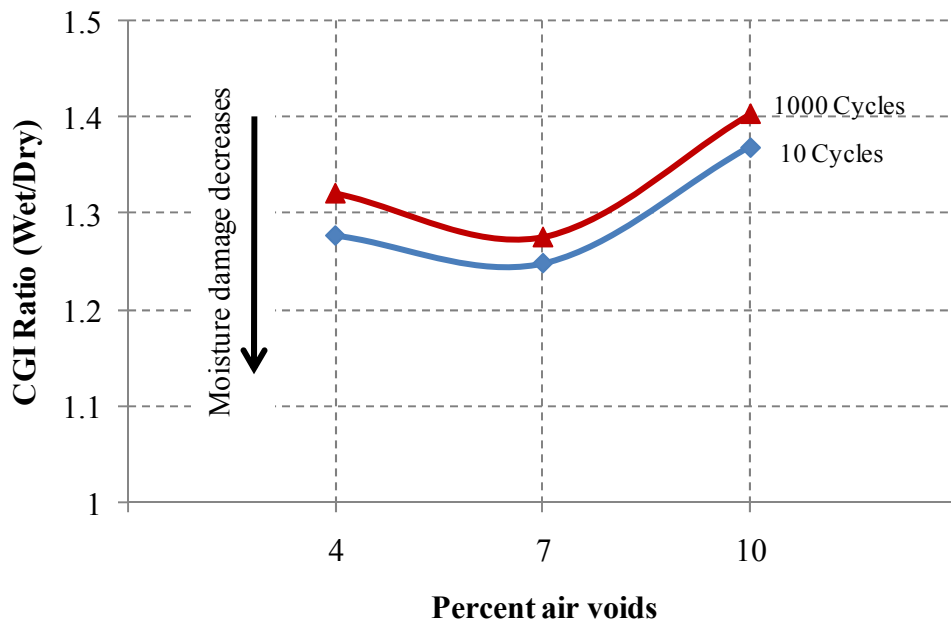
Figure 3-21. Crack Growth Index (Wet/Dry) versus Percent Air Voids.

SUMMARY

In this chapter, the resistance of asphalt mixtures with different percent air voids to moisture damage was evaluated by using a fracture mechanics approach. This approach accounts for fundamental material properties which include the viscoelastic properties, pseudostrain dissipated energy, tensile strength, and the adhesive bond surface energy of asphalt mixture. Dry and wet test asphalt mixtures specimens were evaluated. A crack growth index was used to quantify the damage of the test specimens. The dry samples performed better than the wet ones at each percent air voids. The test specimens with less percent air voids performed better than the ones with higher percent air voids. The detrimental effect of moisture at 7 percent air voids specimens was the least compared to 4 and 10 percent air voids specimens.

The crack growth fracture model clearly demonstrates the effect of different percent air voids on the performance of asphalt mixtures. In addition, the model shows that the detrimental effect of moisture was the greatest at a higher percent air voids, 10 percent. These results show the importance of compaction level on the performance of asphalt mixtures. Effective compaction results in less percent air voids and provides better performance. In addition, the fracture mechanics approach presented in this chapter is a valuable method to evaluate different asphalt mixture designs and select the one with good resistance to moisture damage.

CHAPTER 4

DISCRETE ELEMENT MODELS OF MECHANICAL PROPERTIES OF ASPHALT MIXTURES*

INTRODUCTION

Air voids play an important role in the performance of asphalt mixtures as seen in Chapter 3. This chapter focuses on investigating the air void effect of the mechanical properties of the asphalt mixtures using Discrete Element Models (DEM). Laboratory samples and field cores were evaluated. Test specimens were scanned using X-ray CT to obtain the images of the microstructure of the air void levels. In the simulation of mechanical properties of the asphalt, two-dimensional (2D) and three-dimensional (3D) discrete element models were prepared to evaluate the performance of the mixtures. In the 2D models, both vertical- and horizontal-cut images of the 3D specimen were used to evaluate the different air void levels. In addition, the relationship between the mixture modulus versus the air void levels was investigated.

SCOPE

This study focuses on the effects of different air void levels on asphalt mixtures. The application of the DEM approach was limited to the uniaxial, biaxial, and triaxial compression test. The 2D and 3D microstructures of the asphalt mixture were obtained with the X-ray CT technique. The DEM models were based upon the microstructures of the mixtures.

BACKGROUND OF MICROMECHANICAL MODELS

The micromechanical modeling technique has been successfully used in the past decade. A unified theory for predicting the overall behavior of composite materials was

_____

*Reprinted with the permission from "Microstructural and Micromechanical Properties of Field and Lab-Compacted Asphalt Mixtures" by You, Z., Adhikari, S., Masad, E., and Dai, Q., 2009, *Journal of the Association of Asphalt Paving Technologists*, AAPT, Vol. (78).

proposed to analyze the mechanical behavior of the materials (Aboudi 1991; Aboudi 2004). The cell method was used to predict the strength and fatigue failure of composite materials. A basis for research activity on the micromechanics of heterogeneous materials was provided by Nemat-Nasser and Hori (1999).

Most current micromechanical models for the asphalt mixture have been used to predict asphalt mixture's mechanical properties based upon the ingredients (Li et al. 1999; Papagiannakis et al. 2002). Based upon progress of the other researchers, a microstructure-based finite element model for the asphalt mixture (a heterogeneous material) was developed (Dai et al. 2006; Dai and You 2006). Multiphase asphalt mixture materials, including aggregates and mastic, were divided into different subdomains. The complex modulus of the mixture was then predicted by compression tests (Dai and You 2006). The comparison between the finite element model prediction and laboratory measurement indicated that the predictions were reliable for the asphalt mixtures.

The Discrete Element Method was applied to the particle flow of granular materials. The granular medium is represented by an assembly of discrete blocks which can be considered as rigid or deformable. The method is based on the formulation and solution of the equations of motion or deformation of these discrete blocks and the contacts between them. The contact must be identified by proper constitutive models during the entire deformation or motion process. This study involves the use of a commercially available discrete element program called Particle Flow Code (PFC) in Two Dimensions or PFC2D (Itasca 2004a) and Three Dimensions or PFC3D (Itasca 2004b).

Buttlar and You (2001) proposed a microfabric approach to model asphalt mixture using the discrete element methods, where various material phases (i.e., aggregates and mastic) in the asphalt mixture were modeled with bonded clusters of 2D discrete elements. You et al. (2008) predicted the asphalt mixture modulus across a range of temperatures and loading frequencies using 3D discrete element models.

TEST SPECIMENS AND X-RAY CT

Three SGC laboratory specimens and eight field cores were evaluated in this study. The laboratory specimens are 6.5 inches (165 mm) in height by 6 inches (150 mm)

54

in diameter and prepared using TxDOT Type C mixture with PG 64-22 binder and crushed river gravel aggregate. During the laboratory compaction, temperatures of the top plate, base plate, and mold were varied according to Table 4-1. The field cores were recovered from FM 649 in the Laredo District, where a 2-inch thick Type C mixture was placed on this highway. The mixture contained limestone from the Martin Marietta Beckmann quarry in San Antonio. The mixture contained 4.9 percent PG 76-22 binder from Valero asphalt. The location of these cores and percent air voids are presented in Table 4-2.

The X-ray CT imaging was applied in this study to provide geometric information to represent asphalt concrete in the DEM simulations and to provide microstructure for the 3D quantification of particle kinematics in experiments. The test specimens were scanned using the X-ray CT to estimate the percent air voids at different depths of the specimens. Horizontal images were analyzed for each specimen. During image processing and image analysis, grey images were transferred into two phases, the aggregate/binder phase and the air voids phase. Images were converted into the two phases according to a threshold segmenting of each element.

Table 4-1. Compaction Data of Laboratory Specimens.

Specimen ID	C1-2	C2-2	C3-2
Compaction Temperature (°C)	122	122	122
Top Plate Temperature (°C)	30	30	122
Mold Temperature (°C)	122	152	122
Rice Specific Gravity $G_{mm,}$ gm/cc	2.414	2.414	2.414
Asphalt Binder PG Grade	64-22	64-22	64-22
Air Void, %	10.85	10.36	12.18
Specimen height (mm)	165	165	164
Horizontal images slices (total number)	165	165	164

Table 4-2. Location of Field Cores.

Core ID	Air Void %	Gmm	Location	Horizontal image
5-1	13	2.427	Near longitudinal joint	40
6-1	13.29	2.427	Center of paving lane	42
6-2	12.52	2.427	Left wheel path	40
7-1	13.77	2.427	Right wheel path	40
10-2	13.96	2.427	Near longitudinal joint	52
11-2	12.16	2.427	Center of paving lane	50
11-7	11.39	2.427	Left wheel path	53
12-2	11.78	2.427	Right wheel path	50

MICROMECHANICAL MODEL DESCRIPTION

After the asphalt mixture microstructure was captured using X-ray CT, the images were manipulated using image processing techniques and reconstructed into an assembly of 3D DEM. Image processing techniques were used to identify the mixture (aggregate and binder) and air voids within the images. In this section, the preparation of asphalt mixture using two-dimensional and three-dimensional discrete element models is discussed with imaging technology. The entire 3D and 2D DEM preparations are illustrated in Figure 4-1.

In the discrete element approach, the complex behavior of a material can be simulated by combining simple contact constitutive models with complex geometrical features. Shear and normal stiffness, static and sliding friction, and inter-particle cohesion are three of the simpler contact models that can be employed. The stiffness model was selected to use in this study. For a linear contact model, the contact stiffness is computed by assuming that the stiffness of the two contacting entities acts in series. The force-displacement law of the two elements in contact can be represented using different constitutive laws.

DEM SIMULATION OF BIAXIAL TEST AND TRIAXIAL TEST

The DEM model was simulated on a compression test by confining the stress environment. Four walls were confined for 2D as a biaxial test, and six walls were

confined for 3D as a triaxial test. The walls were made longer than necessary to allow for large amounts of strain to occur during the test. Walls interact with balls, not with one another. The axial compressive force was applied to the top of the specimen with constant speed. The 2D specimens are computed by the biaxial test, and the 3D specimens are computed by the triaxial compression test. In this study, the stiffness model was used as a contact model. The expression of the apparent Young's modulus E of the 3D assembly is a function of the input normal stiffness K_n.

The specimen was loaded by specifying the velocities of the top and bottom walls. The stress was computed by taking the average wall forces and dividing by appropriate areas. Throughout the loading process, the confining stress was kept constant by adjusting the radial wall velocity using a numerical servo-mechanism. The simulation was completed when a specific axial strain level was reached. The modulus was computed from the plots of axial deviator stress (i.e., the difference between axial stress and confine stress) versus axial strain. Contact deviator stress histories and the strain histories were traced to capture the macro and micromechanical responses in the specimens. The modulus was computed from the plots of axial deviator stress versus axial strain. The elastic properties of the specimen can be determined by performing a loading/unloading test under elastic conditions. Since the confining stress is constant, the test can be used to measure the initial Young's modulus.

In this study, the lab tests were completed within the viscoelastic range. In the discrete element modeling, the correspondence principle (Flügge 1975) was used to bridge the linear elastic and viscoelastic behavior through Laplace transformation. This correspondence can be made by taking an appropriate transformation of the governing field and boundary equations of the viscoelastic problems. It is valid to determine the viscoelastic properties from elastic properties for the scope of this study (You and Dai 2007). The simulation using DEM on the viscoelastic model was time consuming. Therefore, it becomes very difficult to simulate dozens of loading cycles as with lab tests. You et al. (2008) predicted the asphalt mixture modulus across a range of temperatures and loading frequencies using 3D discrete element models under uniaxial compressive loads.
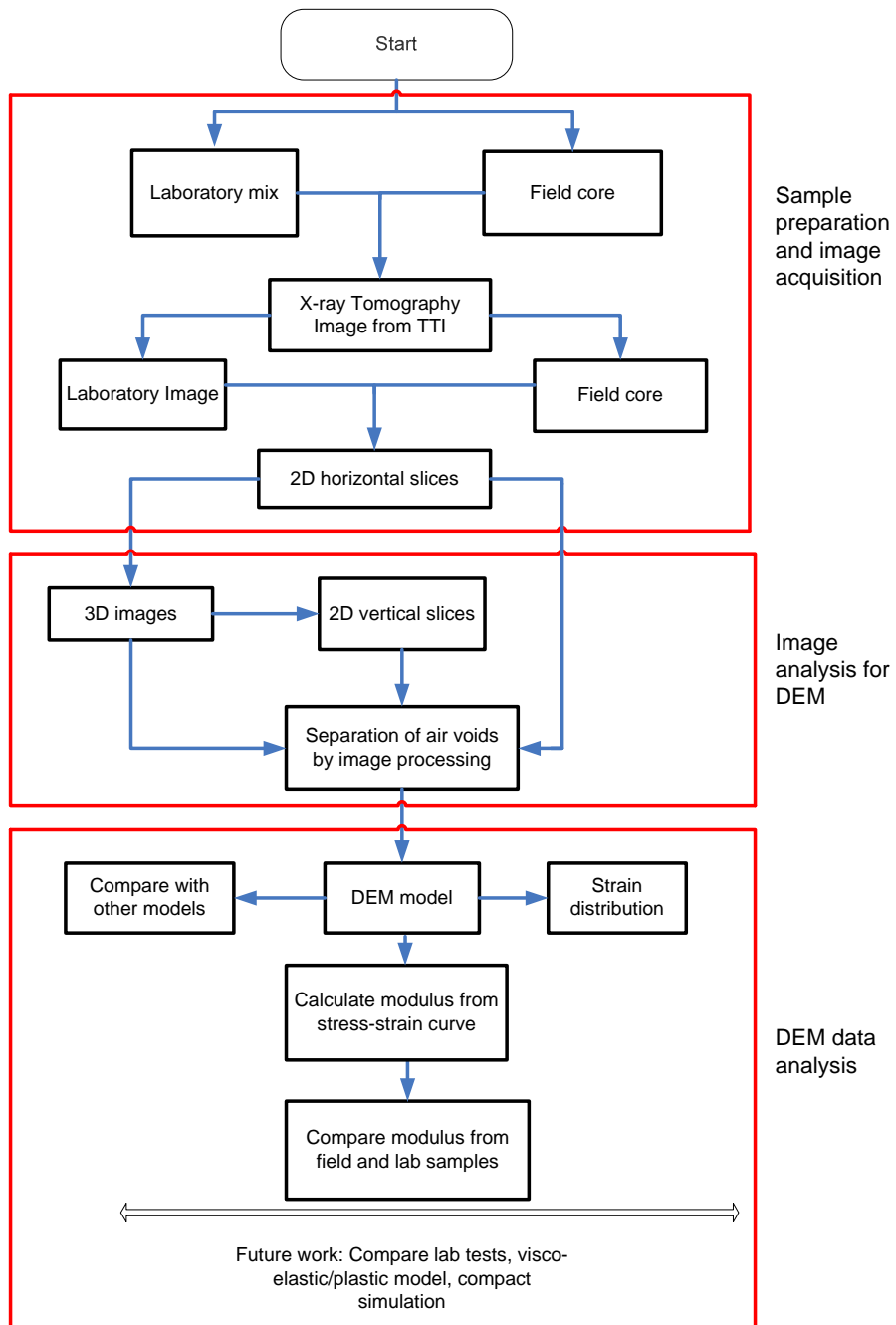
Figure 4-1. Illustration of Image Processing and DEM Modeling Micromechanical Model Description for Asphalt Mixture Specimens.

MICROSTRUCTURE RECONSTRUCTION

In order to examine the stiffness of the asphalt mixture, 2D and 3D discrete element models were used to predict the mixture moduli of the asphalt mixture at different air voids levels. The 3D model was composed of a number of 2D discrete element layers. Both 2D and 3D models were generated using regular packing balls/spheres. The 2D DEM was generated from the vertical and horizontal orientation of the 3D cylinder-shaped specimen as shown in Figure 4-2.

Y1, Y2, Y3, Y4, Y5

b) 2D Vertical Orientation

a) 3D Model

X1
X2
X3
X4
X5

c) 2D Horizontal Orientation
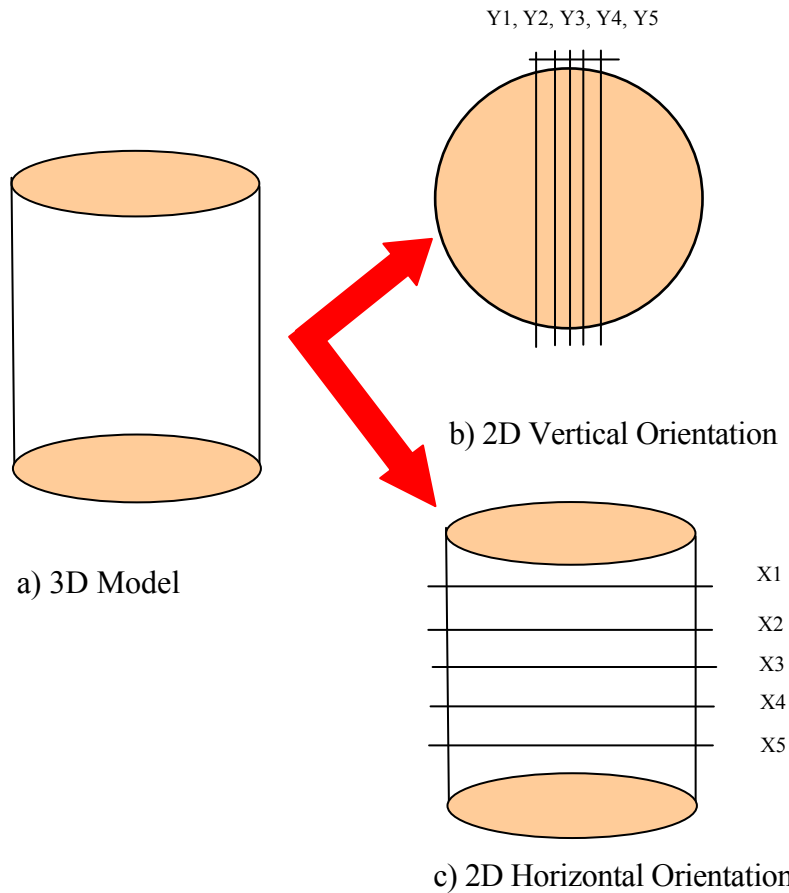
Figure 4-2. Vertical and Horizontal "Cut" of the X-ray Images for the 2D Vertical and Horizontal Models.

3D MODEL PREPARATION

The 3D rectangular prism-shaped specimen was used with a length of 50 mm, width of 50 mm, and depth of 164 mm on the DEM simulation. The radius of each sphere was 0.5 mm. There were a total of 410,000 spheres in this 3D asphalt mixture specimen without air voids. Figure 4-3 shows the illustration of the 3D DEM model that was captured from a horizontal layer of an X-ray CT image. The black color is the asphalt mixture, and the white color is the air voids. The coordinates of the asphalt mixture were used in the DEM simulation. The air voids were removed from the model during the simulation. The discrete element models were constructed using regular packing spheres.

a) 3D Visualization of X-Ray CT Images b) 3D DEM Model Illustration

Figure 4-3. 3D Model Preparation.

2D DEM SIMULATION TO SHOW THE EFFECTS OF THE VERTICAL ORIENTATION

The vertical orientation of the asphalt specimen was captured using image analysis by virtually "cutting" a stack of 2D horizontal images. The 2D vertical orientation was used for the DEM simulation. The 2D rectangular-shaped specimen was

generated having a height of 512 units (or 150 mm) and a width of 512 units (or 150 mm) from the images. The radius of each ball (discrete element) was 0.5 unit (0.15 mm). There were a total of 262,144 balls in the digital or virtual specimen. The vertical orientation of the 3D specimen is 71 mm, 73 mm, 75 mm, 77 mm, and 79 mm from the surface of the specimen. There were a total of 15 vertical slices from the 3 specimens. The air voids of the vertical images were calculated using Matlab software. Figure 4-4 shows the 2D air void distribution in the DEM in different replicates of 3D specimens for which the measurements are compared. The inner 2D sections have lower air voids than the outer sections. The modulus of the vertical orientation of the specimen was predicted using DEM simulation. Figure 4-5 shows the normalized modulus of the vertical orientation.   The modulus of an asphalt mixture is considered to be unity in the absence of any air void. In other words, when there is no existence of air void, the matrix of the model is in fact a one-phase model, and the modulus of the model should be 1.0 when the input is 1.0. When the air void exists, the modulus of the model becomes less than 1.0 when the modulus of the matrix is 1. In the following sections, the normalized modulus is provided for all the 2D and 3D models in order to study the air void effects.

2D DEM SIMULATION TO SHOW THE EFFECTS OF THE HORIZONTAL ORIENTATION

The horizontal orientation of the asphalt specimen was obtained from horizontal slices of X-ray CT images. The total of 18 horizontal images was used for DEM simulation usin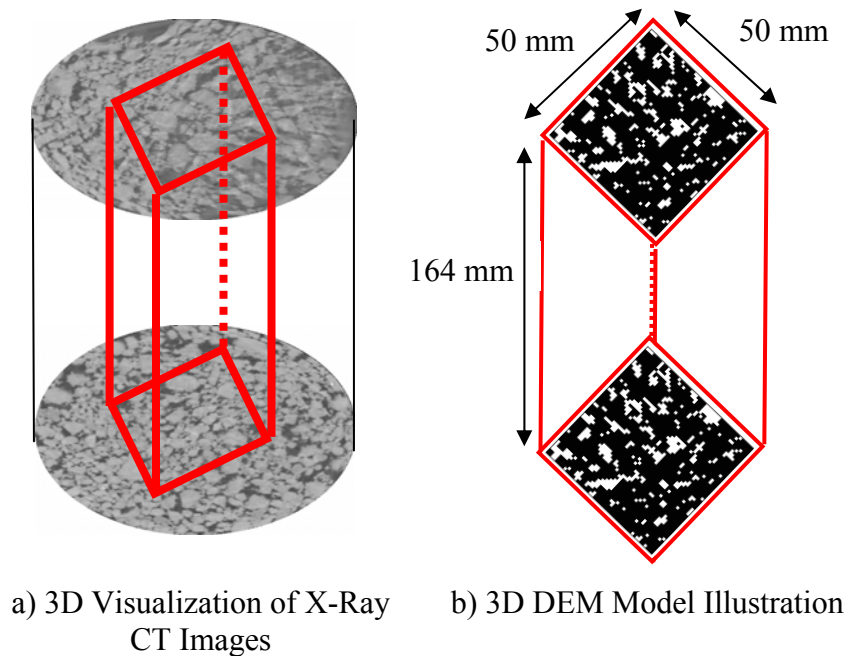g 3 specimens. The horizontal orientation is obtained by "cutting" the specimen at height 15 mm, 50 mm, 75 mm, 100 mm, 125 mm, and 150 mm from the top surface of the specimen to the bottom. These 2D horizontal images were used for DEM simulation. The 2D rectangular shaped specimen was generated with the height of 50 mm and width of 50 mm from the images. The radius of each ball (discrete element) was 0.5 mm. The air voids of the horizontal images are calculated using Matlab software. Figure 4-6 shows the calculated and measured air voids of the horizontal orientation. As seen from the figure, the air void levels are different depending on the locations of the "cut". The top and bottom 2D sections have higher air voids than the middle sections. The modulus of the vertical orientation of the specimen was predicted using DEM simulation.

61

Figure 4-7 shows the modulus prediction of the 2D horizontal orientation of corresponding air void levels. It shows that the lower the air voids, the higher the moduli, and vice versa.

Figure 4-4. Air Void of the Vertical Section of the Three Specimens (2D Models).
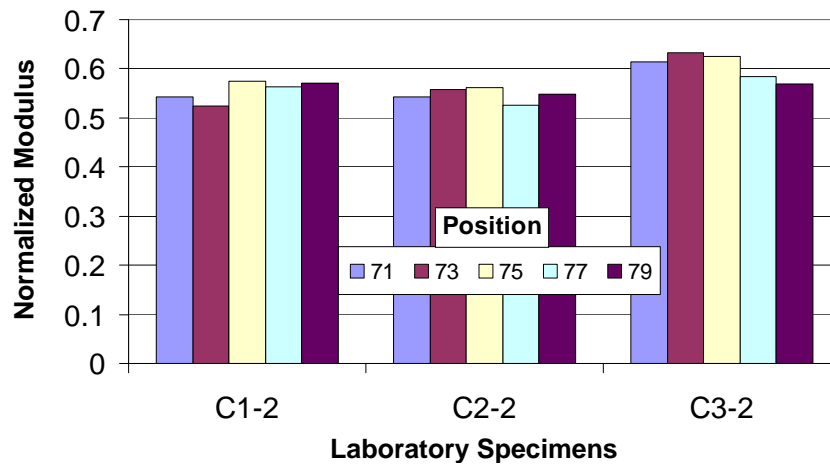
Figure 4-5. Normalized Modulus of the Vertical Section of Three Specimens (2D Models).
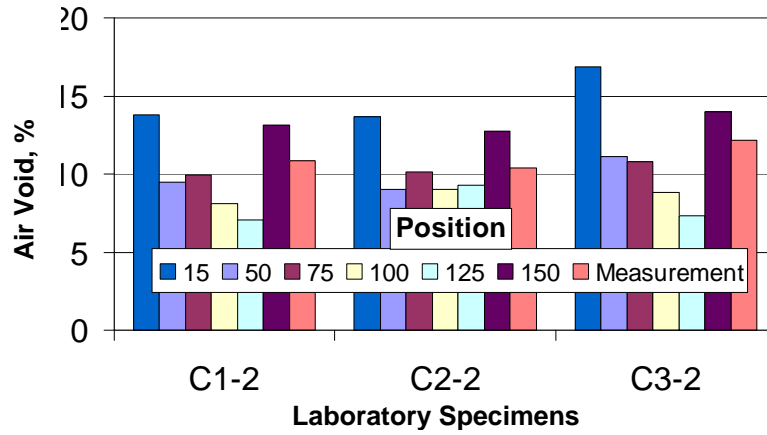
Figure 4-6. Air Void of the Horizontal Section of the Specimens.
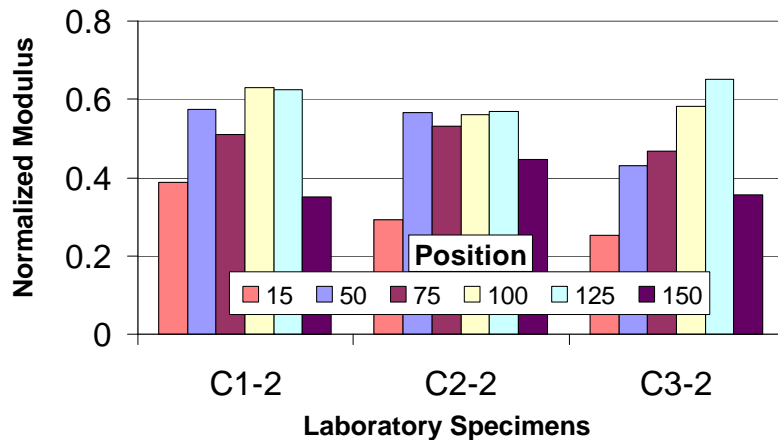
Figure 4-7. Normalized Modulus of the Horizontal Section of the Specimens (2D Models).

COMPARE 3D MODELS, 2D VERTICAL ORIENTATION MODELS, AND 2D HORIZONTAL ORIENTATION MODELS

Compressive test simulations were conducted using the 2D and 3D discrete element models. The modulus of the asphalt mixture was predicted as described before. In this section, the 2D and 3D discrete element models are discussed to compare whether

the 3D models yield better predictions of the asphalt mixture modulus. As the air void content increased, the mixture modulus decreased.

Figure 4-8a shows the relationship of the normalized modulus with corresponding air voids of 3D, 2D horizontal layer, and 2D vertical layer. In general, models with higher air void yield a lower modulus. The modulus of an asphalt mixture is considered to be unity in absence of any air void. An R^2 of 0.9548 was obtained for the 3D models. Only three lab specimens were scanned using the X-ray CT, and therefore only three 3D models were prepared in this study. An R^2 of 0.8001 was obtained for the 15 models using images from horizontal orientation. An R^2 of 0.9306 was obtained for the model obtained from the 18 models using images from horizontal orientation. When compared to the 2D and 3D models, it appears that the 3D models yield the highest modulus, then the 2D models from the vertical orientation, and the 2D models from the horizontal orientation give the lowest for a given air void level. This result was anticipated since many researchers have found that the 3D models are much better in representing the microstructure and mechanical behavior of asphalt mixtures. The 3D models are able to model the aggregate-aggregate interaction, or interlock, which provides superior stone-stone contact in the aggregate skeleton of asphalt mixtures. It is very interesting to see that the DEM results from filed specimens provided R^2 of 0.9044, while all the lab specimens got R^2 of 0.9306 as shown in Figure 4-8b.

Figures 4-9 and 4-10 show the comparison between 2D and 3D models of horizontal and vertical orientations in terms of the air void levels and modulus predicted. It appears that the models from the vertical orientation have closer air void and modulus data compared to the 3D models. The variation of the moduli predicted from the 2D models of vertical orientation is lower than the 2D horizontal ones.

As a summary, the 2D model from vertical orientation had 15 replicates with corresponding air voids, and the 2D horizontal orientation had 18 replicates with corresponding air voids. The 2D horizontal layer predictions have more variation of air voids and modulus prediction than the 2D vertical layer. When the 3D models, 2D vertical models, and 2D horizontal models have similar air voids, the 3D models provided higher moduli than the 2D models. The 2D vertical models yielded higher moduli than the 2D horizontal model for a given air void. The data indicated in the 2D

horizontal model prediction usually yielded inconsistent results (i.e., higher variation) compared with those of a 2D vertical model. A number of researchers agree that the 3D models predict the modulus better than the 2D models, because the 3D models better represent the microstructure of the material than the 2D models. When the air void increased from 0 percent to 10 percent, the modulus decreased 35 percent in the 3D models, compared with 45 percent in 2D vertical model and with 48 percent in 2D horizontal models.

AIR VOID ORIENTATION EFFECT

Air voids play a vital role in asphalt mixture. When the air void content increased, the mixture modulus decreased. The modulus of asphalt mixture depends upon the orientation/distribution of air voids. To analyze the air void sensitivity effect to the modulus, the models were prepared from a real specimen and an idealized specimen with 10 percent air void. The 2D models from the idealized specimen, 2D models vertically "cut" from a real specimen, and 3D models were prepared with 10 percent air voids. The purpose of this study is to analyze the different air void orientation on the asphalt mixture. Table 4-3 shows the dimensions, number of balls and air voids of the idealized specimen, 2D models of a real specimen, and 3D models of a real specimen.

Real specimens were visualized vertically from a 3D specimen. The 2D rectangular-shaped specimen was generated with the height of 512 units (150 mm) and width of 512 units (150 mm) from the images. The radius of each ball (discrete element) was 0.5 units (0.15 mm). There were total of 262,144 balls in the digital specimen. There are 3 replicates of the real 2D specimen. The idealized rectangular-shaped specimens were modeled with the height of 80 mm and width of 40 mm. The radius of each ball (i.e., disk or discrete element) is 1 mm. Therefore, there are a total of 800 balls in the specimen. There are 16 replicates of an idealized 2D specimen. The real and idealized asphalt mixtures were modeled into a 2D DEM simulation.
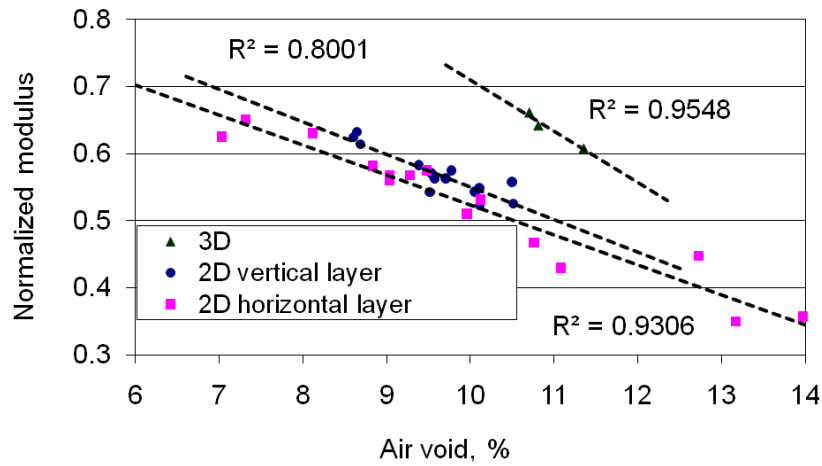
a) Normalized Modulus vs. Air Void of the 3D, 2D Vertical Orientation, and 2D Horizontal Orientation (2D and 3D Models).
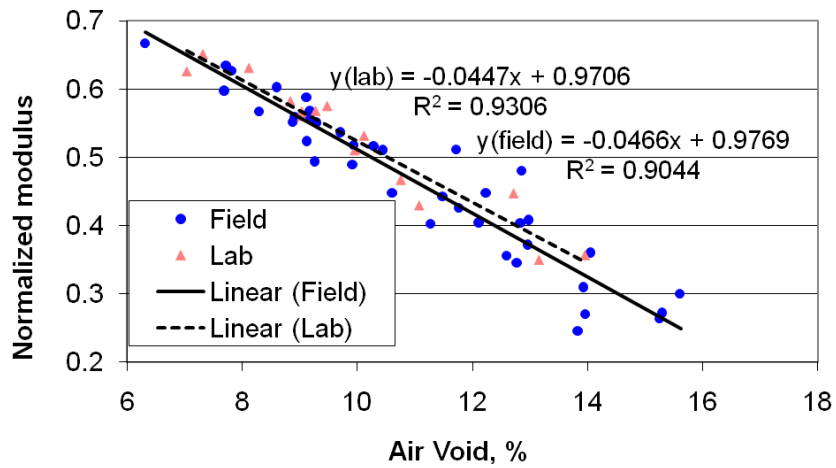
b) Normalized modulus vs. Air Void Levels on DEM Models from Laboratory and Field Specimens.

Figure 4-8. Normalized Modulus vs. Air Void (2D and 3D Models).
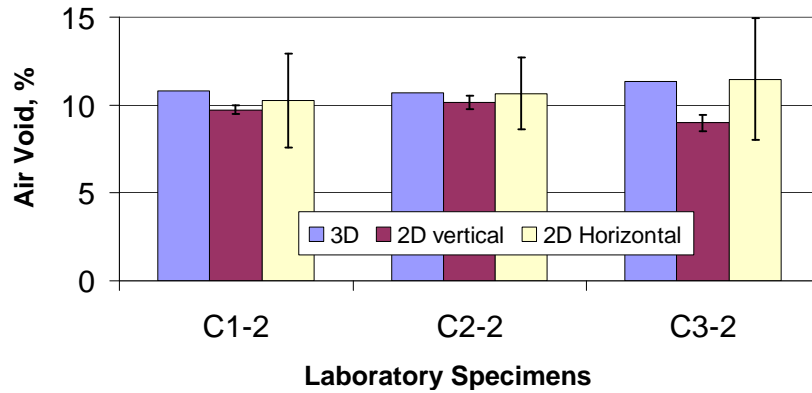
Figure 4-9. Compare Air Void Level of the 3D, 2D Vertical Orientation, and 2D Horizontal Orientation using X-ray CT Images.
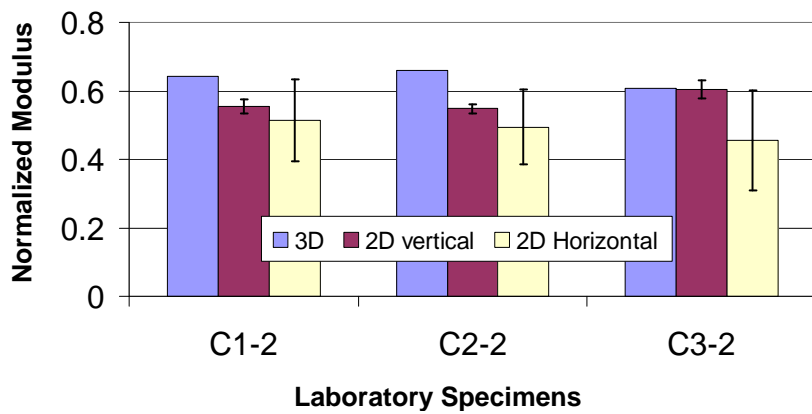
Figure 4-10. Compare Normalized Modulus of 3D, 2D Vertical Orientation, and 2D Horizontal Orientation using X-ray CT Images.

The normalized modulus of the real and idealized asphalt mixture was predicted under 10 percent air void levels using 2D discrete element methods. The modulus prediction of the 3 replicates of real mixtures and the 16 replicates of idealized mixtures were slightly different, i.e., different replicates yield different results, even though the air void level is still 10 percent. The result indicates that the air void orientation in the asphalt mixture affects the mixture modulus. Figure 4-11 shows the average real modulus is slightly higher than average modulus of idealized mixtures. The variation of the moduli

67

predicted from the 2D real models is lower than the 2D idealized model. Figure 4-11 also shows that the 3D mixture model predicts a higher modulus than the 2D mixture model.

Table 4-3. Parameters of 2D and 3D Models.

Specimen	Specimen size (dimension)	Element number	Air void
2D models from the idealized specimen	80 x 40 mm	800	10%
2D models "cut" from a real specimen	150 x 150 mm	262,144	10%
3D model (revised from images of lab specimen)	50 x 50 x 164 mm	410,000	10%
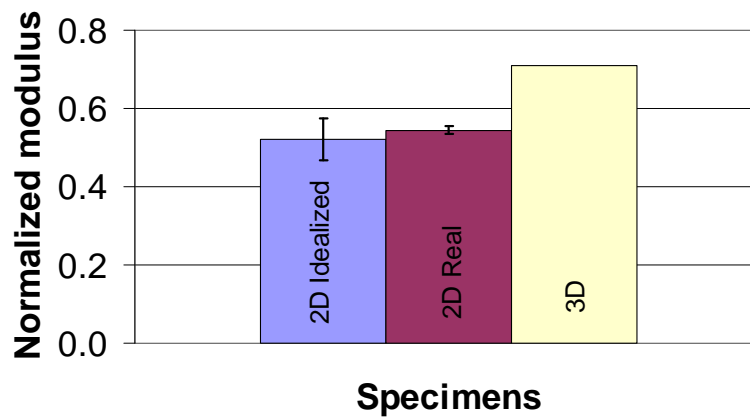
Figure 4-11. Comparing Normalized Modulus of the Idealized Images, Real Images, and 3D Images.

SUMMARY AND CONCLUSIONS

The objective of this part of the study was to investigate the effect of air void on the mechanical properties of the asphalt mixtures under the laboratory and field compactions using discrete element models. The mechanical behavior of asphalt mixture was simulated using both 2D and 3D DEM in order to evaluate the performance of the asphalt mixtures using compression tests on the lab and field compacted specimens. In the 2D models, a biaxial test setup was used to evaluate both vertical and horizontal cut images in order to evaluate the air void structures in different orientations. It was found that the specimens have a lower modulus when the air voids are higher in the specimens for a given air void orientation. Due to the difference of air void distribution in a lab-prepared asphalt mixture specimen and a field cored specimen, the modulus of each thin layer had significant difference depending on the air void structure and the amount of air voids. In addition, the relationship between the mixture modulus and the air void levels was investigated. It was found that the lower the air void, the higher the modulus of the specimen. For a given air void level, the 3D model yield higher stiffness for a given microstructure than 2D models.

The results of this modeling effort demonstrated that the discrete element method can be used to evaluate the effect of air void on the mechanical properties of asphalt mixtures. The results were in agreement with the findings of Chapter 3. Asphalt mixtures with lower percent air voids had a higher modulus than specimens prepared to have higher percent air voids. The discrete element method can be used to investigate the influence of compaction method on mechanical properties. It is recommended to use the 3D model instead of the 2D model in evaluating the mixture mechanical properties as it accounts better for the entire internal structure of asphalt mixtures.

CHAPTER 5

GUIDELINE FOR IMPROVING FIELD COMPACTION

INTRODUCTION

The findings from Report 0-5261-1 and this report showed that typically the air void distribution is not uniform across the paving mat. The air void distribution correlated very well with the compaction effort on the test section. The compaction effort was presented by the number of roller passes and the location of each pass across the mat, referred to as Compaction Index (CI). The efficiency of compaction at a given point is a function of the location of this point with respect to the roller width. A point on the mat closer to the center of the roller is subjected to more effective compaction than a point closer to the edge of the roller. In addition, the air void distribution was found to be influenced by the number of passes of the vibratory and static rollers compared to the pneumatic one. The results also revealed a relationship between the compactability of asphalt mixtures in the field and laboratory. For a given percent of air voids, the compaction effort needed in the field correlated well with the slope of the laboratory compaction curves. A higher compaction effort in the field was associated with a smaller slope of the laboratory compaction curves. Based on these findings, the research team submits some recommendations to improve the field compaction of asphalt mixtures. The proposed recommendations can be applied during the mixture design and the construction stages.

RECOMMENDATIONS DURING THE MIXTURE DESIGN STAGE

It is recommended to use the developed relationship between the slope of the laboratory compaction curve and compaction index to decide on the field compactability during the mixture design stage. This approach will ensure the mixtures can be compacted in the field with required resistance to distresses that are associated with poor compactability. The process of evaluating the compactability is illustrated in Figure 5-1, and it is outlined in the following steps:

71

1) Compact the asphalt mixture using the Superpave gyratory compactor.

2) Plot the compaction curve (percent air voids versus number of gyrations) in a semi log scale (Figure 5-1a).

3) Calculate the slope of the compaction curve between the initial compaction point and the point at 8 percent air voids.

4) Use the relationship in Figure 5-1b to determine the CI.

5) Use Table 5-1 to determine the mixture compactability in the field.

6) If the mixture is in the difficult compactability region, the contractor can choose to adjust the mixture design to improve the mixture compactability or set up a compaction pattern and equipment in the field that can be used to achieve the required compaction level (number of passes, sequence of compaction, frequency, and amplitude of vibratory roller).

The research team is fully aware that the mixture compaction is influenced by the type of equipment, the operations of the equipment, the mat temperature, and the air temperature. The recommendations in Table 5-1 are based on the conditions used in the field projects that were used in this study. However, our results show that the CI concept applied reasonably well for all projects irrespective of the equipment used in these projects. The recommendations in Table 5-1 should be used as initial guidelines as some necessary adjustments can be made later as more field data about the influence of type of equipment and the operational characteristics of the equipment on the results. It should be noted that the required number of passes can be determined as the ratio of the compaction index to the effectiveness factor at a point within the pavement mat.

We did not put recommendations on the field adjustments needed to achieve the desired compaction level if the mixture falls under the "difficult compactability" level. The contractor and highway agency personnel would be in a better position to make the necessary plans and adjustments to achieve compactability given the prevailing site and climatic conditions. However, the fact that a mixture belongs to the "difficult compactability" should be treated as an indication that special efforts will be needed to compact the mixture.

GPS

Control Compaction Pattern

(c)

(d)

Required Compaction Index

Lab Compaction Data

Slope =5.03CI$^{-0.25}$

Slope of Compaction Curve

Compaction Index, CI
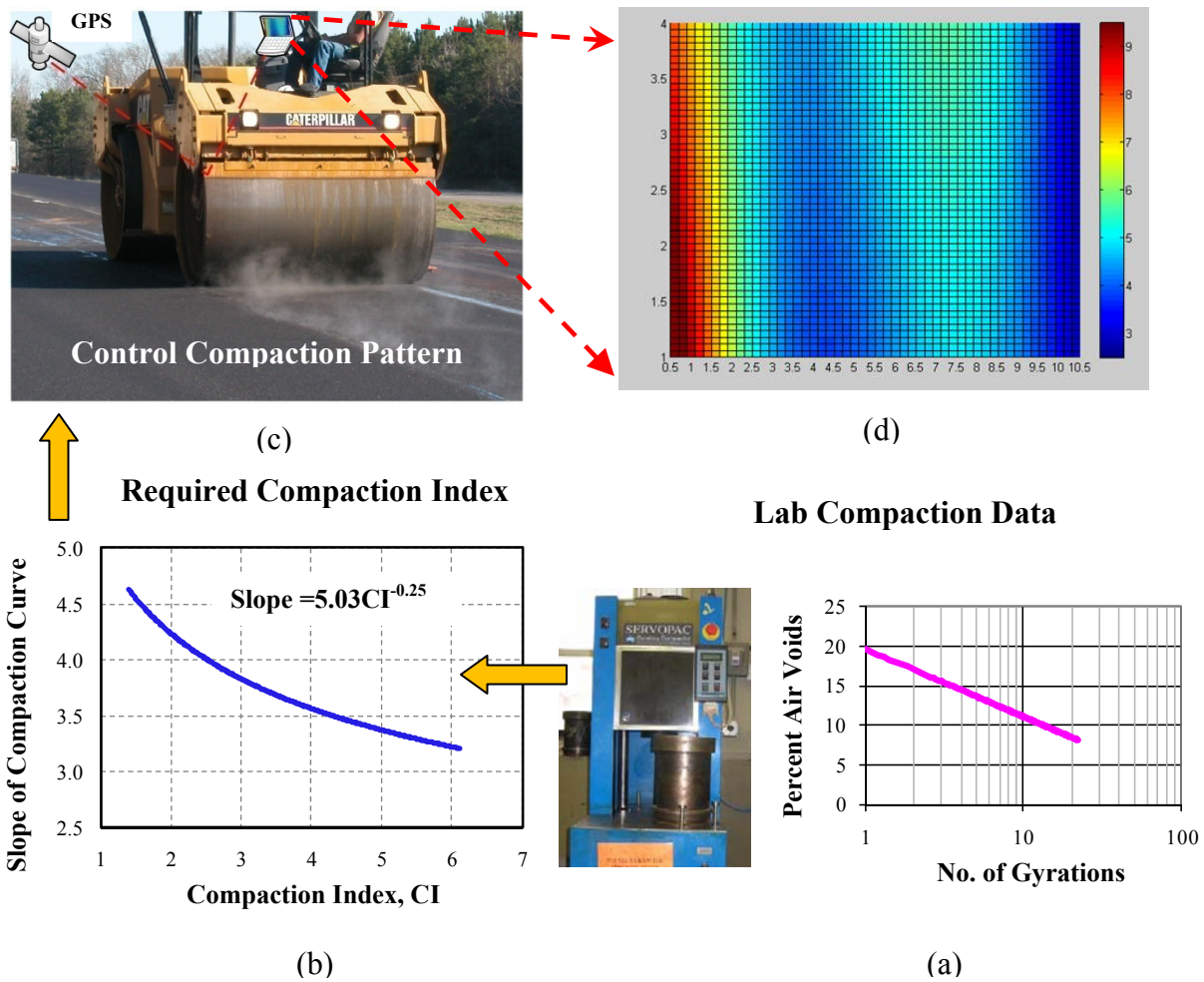
Percent Air Voids

No. of Gyrations

(b)

(a)

Figure 5-1. Evaluating the Compactability Process.

Table 5-1. Recommended Levels for Field Compactability.

CI Value	Compactability Level
<3	Easy Compactability
3-5	Moderate Compactability
>5	Difficult Compactability

RECOMMENDATIONS DURING THE CONSTRUCTION STAGE

The findings showed that the efficiency of a steel wheel roller pass is not uniform across its width. The efficiency in the middle 3 ft of a 7-ft wide roller has the full and uniform effect. This efficiency decreases toward the edges of the roller. Uniform air void distribution was found to be associated with a more uniform compaction index. Researchers recommend the following steps during the construction stage:

1) Overhanging of the roller edge at a distance of about 1.5 ft to 2 ft from the longitudinal joint. This way the longitudinal joint will experience the maximum effectiveness of a given roller pass. Please note that, typically, the edge of the mat or longitudinal joints is subjected to fewer roller passes. Researchers found this overhanging of the roller at the joint can be done without any problem for the restrained joints, but it might reduce the thickness of the mat at the unrestrained or free joints. Consequently, it is recommended to decrease the overhanging of the roller edge to about 1 ft at the unrestrained joints or joints with very steep slope.

2) Overlapping between adjacent passes is recommended to be a minimum of 1.5 ft to 2 ft in order to achieve a uniform density across the width of the roller. This overlapping of successive roller passes will ensure that every point across the mat width experiences a minimum compaction index.

3) A compaction roller equipped with Geographic Information System (GIS) and a simple software program can be used to guide the operator during the construction to achieve the desired coverage. A system can be developed such that the operator can see the real-time map of compaction index across the width during compaction (Figure 5-1d). The operator can accordingly adjust the successive pass and/or overlap to achieve uniform CI and uniform density across the mat.

4) Use of the pneumatic tire compactor in the breakdown compaction would help in achieving compaction in harsh mixtures that are difficult to compact.

CHAPTER 6

CONCLUSIONS AND RECOMMENDATIONS

CONCLUSIONS

A little effort was devoted in the past to study the factors that affect the uniformity and level of compaction of asphalt pavements in the field. This study aimed at providing such understanding in order to achieve more uniform asphalt pavements with better performance. The effect of different levels of compaction on the mechanical properties of asphalt pavements was also examined using a fracture mechanics approach and Discrete Element Models. The fracture mechanics approach accounts for fundamental material properties of asphalt mixtures, while the DEM models was used to simulate the mechanical behavior of asphalt mixtures. The following points summarize the main findings from this report.

Evaluation of Field Compaction

- The results of the three test sections evaluated in this part of the project agreed with the findings from Report 0-5261-1.

- The air void distribution correlated well with the compaction effort across the mat. The compaction effort was found to be a function of number of roller passes and the location of each pass across the mat. Therefore, a new index referred as the Compaction Index is proposed to quantify the compaction effort at any point in the pavement. This index is the summation of the multiplication of each pass with an effectiveness factor. The effectiveness factor at a point is a function of the location of the point with respect to the roller width. A point on the mat closer to the center of the roller is subjected to more effective compaction than a point closer to the edge of the roller.

- The CI is used to study the compactability of asphalt mixtures in the field. The CI correlated well with the slope of the laboratory compaction curves. Asphalt mixtures with a higher slope in the laboratory needed less CI in the field to achieve the same percent air void.

75

- It is demonstrated that the CI is useful to set up the compaction pattern in achieve uniform percent air voids. A more uniform CI corresponds to more uniform air voids across the mat.

- In most of the test sections, it was found that the middle part (across the depth) of the mat is more compacted than the top and bottom parts.

Fracture Analysis of Moisture Damage

- The resistance of asphalt mixtures with different percent air voids to moisture damage was evaluated by using a fracture mechanics approach in which a crack growth index was used to quantify the damage of the test specimens.

- The analysis approach confirmed that the dry samples performed better than the wet ones at each percent air voids.

- The test specimens with less percent air voids performed better than the ones with higher percent air voids.

- The detrimental effect of moisture was the lowest at 7 percent air voids compared with 4 and 10 percent air voids specimens.

Discrete Element Models of Mechanical Properties

- The effect of air void on the mechanical properties of asphalt mixtures was investigated using discrete element models. The performance of asphalt mixtures was simulated using both 2D and 3D DEM.

- For a given air void orientation, test specimens with less percent air voids have a higher modulus compared to specimens at higher percent air voids.

- For a given air void level, the 3D model yield higher stiffness for a given microstructure than 2D models.

RECOMMENDATIONS

The following are main recommendations based on the findings of this study:

1. Verify the relationship between laboratory compaction data and field compaction by compacting more mixtures under different site and climatic

conditions. This additional effort will also validate the effectiveness factors distribution and compaction index concept.

2. Develop a setup that can be used in the compaction equipment to monitor and record the position of the roller with respect to the mat and the number of passes across the different points in the mat. This data can be used to plot the Compaction Index across the mat. The equipment operator can then adjust the compaction pattern to achieve a uniform CI and consequently a uniform distribution of air voids.

3. Evaluate the effect of different compaction rollers and operational characteristics on the values of the compaction index, and make adjustments to the recommendations in Table 5-1 to account for the type of equipment is necessary. Our initial results suggest that the CI value is not very sensitive to the type of equipment.

REFERENCES

Aboudi, J. (1991). "Mechanics of Composite Materials, a Unified Micromechanical Approach," *Elsevier*, 14-21.

Aboudi, J. (2004). "The generalized method of cells and high-fidelity generalized method of cells micromechanical models – a review," *J. Mech. Adv. Mater. Struct,* Vol. 11, 329-366.

American Association of State Highway and Transportation Officials (AASHTO). (2002a). "Bulk Specific Gravity of Compacted Asphalt Mixtures Using Saturated Surface-Dry Specimens." T 166. Standard Specifications for Transportation Materials and Methods Sampling and Testing, American Association of State Highway and Transportation Officials, Washington, D.C.

American Association of State Highway and Transportation Officials (AASHTO). (2002b). "Preparing and Determining the Density of Hot-Mix Asphalt (HMA) Specimens by Means of the Superpave Gyratory Compactor." *T312*. Standard Specifications for Transportation Materials and Methods Sampling and Testing, American Association of State Highway and Transportation Officials, Washington, D.C.

American Association of State Highway and Transportation Officials (AASHTO). (2007)."Standard Method of Test for Resistance of Compacted Asphalt Mixtures to Moisture-Induced Damage." T 283. Standard Specifications for Transportation Materials and Methods Sampling and Testing, American Association of State Highway and Transportation Officials, Washington, D.C.

Arambula, E. (2007). "Influence of Fundamental Material Properties and Air Void Structure on Moisture Damage of Asphalt Mixes." Ph.D. Dissertation, Texas A&M University, College Station, Texas.

Buttlar W.G., and You, Z. (2001). "Discrete Element Modeling of Asphalt Concrete: A Micro-Fabric Approach," *Journal of the Transportation Board*, Washington, D.C., Vol. 1757.

Caro, S., Masad, E. Bahsin, A., and Little, D.N. (2007). "Moisture Susceptibility of Asphalt Mixtures, Part 1: Mechanisms," *International Journal of Pavement Engineering*, submitted for publication.

Consuegra, A., Little, D.N., Quintus, H.V., and Burati, J. (1989). "Comparative Evaluation of Laboratory Compaction Devices Based on Their Ability to Produce Mixtures with Engineering Properties Similar to Those Produced in the Field," In *Transportation Research Record* 1228, TRB, National Research Council, Washington, D.C., pp. 80-87.

Corps of Engineers (2000). "Hot-Mix Asphalt Paving Handbook 2000," AC 150/5370-14A, US Army Corps of Engineers, Washington, D.C.

Dai, Q., Sadd, M.H., and You, Z. (2006). "A Micromechanical Finite Element Model for Viscoelastic Creep and Viscoelastic Damage Behavior of Asphalt Mixture," *International Journal for Numerical and Analytical Methods in Geomechanics*, Vol. 30, 1135-1158.

Dai, Q., and You, Z. (2006). "Prediction of Creep Stiffness of Asphalt Mixture with Micromechanical Finite Element and Discrete Element Models," *Journal of Engineering Mechanics*, ASCE, Vol. 133 (2), 163-173.

Flügge, W. (1975). "Viscoelasticity," Berlin, Springer.

Harvey, J., and Monismith, C.L. (1993). "Effects of Laboratory Asphalt Concrete Specimen Preparation Variables on Fatigue and Permanent Deformation Test Results Using Strategic Highway Research Program A-003A Proposed Testing

Equipment," In *Transportation Research Record* 1417, TRB, National Research Council, Washington, D.C., pp. 38-57.

Howson, J., Masad, E., Bhasin, A., Branco, V., Arambula, E., Lytton, R., and Dallas, L. (2007). "System for the Evaluation of Moisture Damage Using Fundamental Material Properties." Research Report FHWA/TX-07/0-4524-1, TTI, College Station, Texas.

Image-Pro® Plus (1999). Media Cybernetics, L.P. Georgia, M.D. Version 4.1.

Itasca Consulting Group, PFC 2D Version 3.1. (2004a). Minneapolis, Minnesota.

Itasca Consulting Group, PFC 3D Version 3.1. (2004b). Minneapolis, Minnesota.

Li, G., Li, Y., Metcalf, J.B., and Pang S.S. (1999). "Elastic modulus prediction of asphalt concrete," *Journal of Materials in Civil Engineering*, Vol. 11(3), 236-241.

Lytton, R., Uzan, J., Fernando, E., Hiltmen, D., and Stoffels, S. (1993). "Development and Validation of Perfomance Prediction Models and Specifications for Asphalt Binder and Paving Mixtures," *SHRP A-357*, Strategic Highway Research Program. Washington, D.C.

Masad, E., Al-Omari, A., and Lytton, R. (2006a). "Simple Method for Predicting Laboratory and Field Permeability of Hot Mix Asphalt," In *Transportation Research Record* 1970, TRB, National Research Council, Washington, D.C., pp. 55-63.

Masad, E., Zollinger, C., Bulut, R., Little, D., and Lytton, R. (2006b). "Characterization of HMA Moisture Damage Using Surface Energy and Fracture Properties," *Journal of the Association of Asphalt Paving Technologists*, Vol. 75, pp. 713-748

Masad, E., Kassem, E., and Chowdhury, A. (2008). "Using Imaging Technology to Improve the Laboratory and Field Compaction of Hot Mix Asphalt." Technical Report Number 0-5261-1, Texas Transportation Institute, Texas A&M University, College Station, Texas.

Matlab Software (2004). The MathWorks Inc., Natick, Massachusetts, Version 7.

Nemat-Nasser, S., and Hori, M. (1999). "Micromechanics: Overall Properties of Heterogeneous Materials," 2nd ed. 1, North-Holland, Amsterdam.

Papagiannakis, A.T., Abbas, A., and Masad, E. (2002). "Micromechanical analysis of viscoelastic properties of asphalt concretes," *Transportation Research Record*, Vol. 1789, pp: 113-120.

Peterson, B., Mahboub, K., Anderson, M., Masad, E., and Tashman, L. (2004). "Comparing Superpave Gyratory Compactor Data to Field Cores," *Journal of Materials in Civil Engineering, ASCE,* Vol. 16(1), pp. 78-83.

Roberts F.L., Kandhal, P.S., Brown, E.R., Lee D., and Kennedy, T.W. (1996). "*Hot Mix Asphalt Materials, Mixture Design and Construction*," National Asphalt Pavement Association, Research and Education Foundation, Lanham, Maryland.

Si, Z. (2001). "Characterization of Microdamage and Healing of Asphalt Concrete Mixtures." Ph.D. Dissertation, Texas A&M University, College Station, Texas.

Tashman, L., Masad, E., Peterson, B., and Saleh, H. (2001). "Internal Structure Analysis of Asphalt Mixes to Improve the Simulation of Superpave Gyratory Compaction to Field Conditions," *Journal of the Association of Asphalt Paving Technologists,* Vol. 70, pp. 605-645.

Wolf, P., and Ghilani, C. (2002). Elementary Surveying: An Introduction to Geomatics, 10th Ed., Prentice Hall, Upper Saddle River, New Jersey.

You, Z., and Dai,Q. (2007). "Dynamic Complex Modulus Predictions of Hot-Mix Asphalt Using a Micromechanical-Based Finite Element Model," *Canadian Journal of Civil Engineering*, Vol. 34(12), pp. 1519-1528.

You, Z., Adhikari, S., and Kutay, M.E. (2008). "Dynamic Modulus Simulation of the Asphalt Concrete Using the X-ray Computed Tomography Images," *Materials and Structures/Materiaux et Constructions*, Vol. ISSN 1359-5997 (Print) 1871-6873 (Online), DOI 10.1617/s11527-007-9303-4.